

Beyond the Next Port: A Multi-Task Transformer for Forecasting Future Voyage Segment Durations

Nairui Liu, Fang He*

Department of Industrial Engineering, Tsinghua University, Beijing 100084, P.R. China

Xindi Tang

School of Management Science and Engineering, Central University of Finance and Economics, Beijing 100081, P.R. China

Accurate forecasts of segment-level sailing durations are fundamental to enhancing maritime schedule reliability and optimizing long-term port operations. However, conventional estimated time of arrival (ETA) models are primarily designed for the immediate next port of call and rely heavily on real-time automatic identification system (AIS) data, which is inherently unavailable for future voyage segments. To address this gap, the study reformulates future-port ETA prediction as a segment-level time-series forecasting problem. We develop a transformer-based architecture that integrates historical sailing durations, destination port congestion proxies, and static vessel descriptors. The proposed framework employs a causally masked attention mechanism to capture long-range temporal dependencies and a multi-task learning head to jointly predict segment sailing durations and port congestion states, leveraging shared latent signals to mitigate high uncertainty. Evaluation on a real-world global dataset from 2021 demonstrates the proposed model consistently outperforms a comprehensive suite of competitive baselines. The result shows a relative reduction of 4.85% in mean absolute error (MAE) and 4.95% in mean absolute percentage error (MAPE) compared with sequence baseline models. The relative reductions with gradient boosting machines are 9.39% in MAE and 52.97% in MAPE. Case studies for the major destination port further illustrate the model's superior accuracy.

Key words: Maritime logistics, Sailing duration prediction, Future voyage segments, Multi-task learning, Transformer-based model, Segment-level forecasting

1. Introduction

The maritime industry serves as a cornerstone of the global logistics framework and a primary conduit for international commerce (Chu et al. 2024a; Wang et al. 2023). According to *Review of Maritime Transport 2024* published by the United Nations Conference on Trade and Development, maritime transport facilitates approximately 80% of global trade by volume. In 2023, global

* Corresponding author. E-mail address: fanghe@tsinghua.edu.cn.

seaborne trade volumes ascended to 12.292 billion tons, representing an estimated 62.037 trillion ton-miles, thereby solidifying its status as the main artery of global trade ([UNCTAD 2024](#)).

Operational efficiency within this domain is fundamentally predicated on the precision of estimated time of arrival (ETA) predictions. Accurate ETA forecasts empower port managers to optimize berth allocation, crane assignments, and yard space management, while facilitating the proactive synchronization of trucking and rail slots to minimize vessel idle time and cargo dwell durations. From the perspective of carriers, such precision is indispensable for maintaining schedule integrity, ensuring seamless transshipment connectivity, and informing strategic voyage speed adjustments ([Yan et al. 2021](#)). Conversely, the propagation of ETA discrepancies, which is often exacerbated by port congestion or unforeseen systemic disruptions, results in significant operational inefficiencies, characterized by either underutilized berths or excessive vessel queuing at anchorage, both of which lead to resource wastage and degraded transportation throughput ([Chu et al. 2024b](#); [Yang et al. 2024](#)).

Generally, the ETA prediction task in maritime logistics can be decomposed into two distinct components: predicting the remaining sailing duration of the current voyage segment and forecasting the sailing duration for future voyage segments. Contemporary research has focused extensively on the former, essentially estimating the arrival time at the immediate next port for vessels ([Jiang et al. 2025](#)). Recent advancements in deep learning and classical machine learning have significantly improved prediction accuracy beyond traditional vessel schedules and AIS information. However, limited research has investigated the latter task, which remains strategically vital for the ETA prediction of subsequent ports within a liner service ([Noman et al. 2025](#)).

Accurate sailing duration forecasts for future segments offer a critical opportunity for a cascade of medium-to-long-horizon planning for both port managers and vessel carriers. For instance, ports along a liner service can proactively reserve berth windows and labor several calls in advance, while carriers can optimize feeder connections and protect the integrity of transshipment chains. Despite its importance, this task faces fundamental challenges compared to next-port ETA prediction. Specifically, real-time AIS data, which has been proven to be the most significant factor for next-port ETA prediction ([Chu et al. 2025](#)), is inherently unavailable for future voyage segments. Furthermore, the long time horizon between the current vessel stage and future arrivals introduces high uncertainty, rendering models designed for the immediate next port non-transferable to the sailing duration prediction task on future voyage segments. This underscores the necessity for a specialized model architecture designed to handle long-term sailing duration forecasting tasks for future voyage segments.

To address these gaps, we propose shifting the analytical paradigm from a vessel-wise to a segment-wise perspective. While deep learning has shown immense potential in sequence modeling,

existing studies often ignore the time-series patterns inherent in the sailing duration sequence of voyage segments. These historical sequences contain vital changing patterns that are essential for long-term forecasting. As segment sailing durations are tightly associated with the operating state of the destination port, we formulate a joint learning problem to predict both future segment sailing durations and future port congestion states. This multi-task design leverages shared latent signals between sailing durations and port conditions, yielding forecasts that are more robust for maritime planning. The specific contributions of this paper are summarized as follows:

1. We focus on a new prediction task targeting the sailing duration of future voyage segments on liner services, rather than estimating only the remaining time to the next port. This formulation directly supports reliability-oriented planning, such as multi-step berth allocation and downstream coordination across upcoming port calls.
2. We develop a unified sequence-to-sequence (Seq2Seq) transformer-based architecture with a multi-task learning strategy for segment-level sailing duration prediction. To address the lack of real-time AIS on future legs, we transform the view from vessel-level to segment-level to avoid the dependency on AIS data. Key features including segment-level historical sailing duration sequences, port congestion levels, and segment identifier are selected to model each voyage segment. The masked attention mechanism is utilized to capture the long-range time dependency of sailing durations. By jointly predicting sailing durations and destination port congestion levels with multi-task learning strategy, the model captures shared latent signals that govern both sailing behavior and port operating conditions under limited observations.
3. We evaluate the proposed framework on a real-world global sailing record dataset in 2021. Extensive experiments demonstrate that the proposed approach achieves consistently strong predictive accuracy. It outperforms multiple competitive baselines, including gradient boosting models and sequential deep learning models, across segments of various sailing distances and service frequencies.

Figure 1 presents an overview of the proposed framework. The remainder of this paper is organized as follows. Section 2 reviews the related literature and identifies the research gaps addressed in this study. Section 3 describes the data preprocessing pipeline and the proposed model architecture. Section 4 reports the experimental setup and validation results on voyage segments worldwide. Finally, Section 5 concludes the paper with a discussion of limitations and directions for future research.

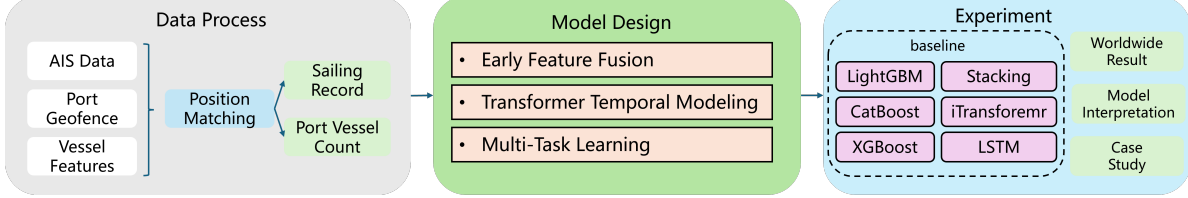


Figure 1 The overall architecture of the ETA prediction and evaluation framework.

2. Literature Review

This study belongs to the ETA estimation problem in maritime transportation. We first review the maritime ETA literature to summarize the main methodological approaches. Given the structural similarities between inland ETA prediction and the maritime setting, we then survey representative inland approaches to extract transferable modeling insights. Finally we clarify the research gap.

2.1. Maritime ETA Prediction

Research on maritime ETA prediction can be mainly divided into two categories, path finding algorithm and data engineering algorithm (Noman et al. 2025). The previous one aims to predict the remaining trajectories from current position to the destination port, afterwards calculating the remaining sailing time based on the predicted vessel trajectory and vessel speed (Alessandrini et al. 2019; Kwun and Bae 2021; Park et al. 2021). Such approaches describe the future behavior of vessels in detail but may suffer from the sparsity of trajectories. In contrast, the latter one tries to predict the result directly without explicitly reconstructing the voyage path (Chu et al. 2024b; El Mekkaoui et al. 2022b; Kolley et al. 2023; Servos et al. 2019; Noman et al. 2021). These methods extract meaningful features from real-time AIS data such as position and speed, cooperated with vessels' static features, to learn nonlinear relationships between features and remaining sailing durations.

Noman et al. (2021) benchmarked three learning paradigms including gradient boosting decision trees (GBDT), multi-layer perceptron (MLP), and gated recurrent unit (GRU) for ETA prediction on inland natural and artificial waterways, and reported that the GRU achieved the best accuracy with RMSE of 8.50 minutes and MAE of 5.92 minutes. Abdi and Amrit (2024) proposed a fusion based deep learning framework for vessel arrival time prediction that integrates multiple data sources including AIS trajectories, vessel attributes, maritime weather, and ocean currents into a unified model. Their architecture first extracts local temporal patterns from each time dependent stream with convolutional neural networks (CNN), then captures long range dependencies via long short-term memory (LSTM) augmented with attention, and finally concatenates static vessel features before dense layers, reporting RMSE of 10.63 and MAPE of 35.11%. Ogura et al. (2021) introduced a two-stage ETA framework that explicitly incorporates future weather information. In the first stage, the route is inferred by selecting historical trajectories whose observed

weather patterns most closely match the forecasting future conditions. In the second stage, the voyage speed is estimated using a Bayesian learning approach. 28% improvement in arrival time prediction accuracy is reported compared with previous methods. [Chu et al. \(2025\)](#) proposed a stacking model framework for ETA prediction that fuses static port call records with dynamic AIS trajectories to reduce the bias of historical actual time of arrival (ATA) and thus to enhance ETA prediction accuracy. With the case analysis of Hong Kong, MAE is reduced by 54.53% and RMSE by 50.14% compared to vessel-reported ETA. [Wenzel et al. \(2023\)](#) designed a three-layer neural network trained on historical AIS trajectories for inland waterways in Netherlands and Germany, and reported accuracy gains of 20.6% for short trips, 4.8% for medium trips, and 13.4% for long-haul trips. [Alessandrini et al. \(2019\)](#) proposed a data-driven method for estimating vessels' times of arrival using historical AIS trajectories. It builds density and direction maps and applies an optimized path-finding algorithm with a statistical speed model to infer routes and travel times from current vessel positions to target ports. Validated on real operational scenarios in Europe, their approach demonstrates clear gains over schedule-based heuristics. [Zhang et al. \(2023\)](#) addressed ETA to pilotage area with heterogeneous sources of data. The temporal convolutional network is selected to extract temporal patterns from sequential AIS data. Experiments on two real-world Singapore datasets yielded MAE less than 4.86 minutes and around 90% of absolute errors within 10 minutes. [Park et al. \(2021\)](#) proposed an AIS-driven ETA system with two stages. In the first stage, possible vessel trajectories are learned through a path-finding module enhanced with reinforcement learning, and in the second stage, speed-over-ground is estimated using a Markov-chain formulation with Bayesian sampling. Experiments on Busan port dataset demonstrate the advantage. [El Mekkaoui et al. \(2022a\)](#) studied ETA prediction for bulk ports by framing the problem as sequence learning over historical AIS data. Multiple deep learning models are trained and compared. Experiments show that these sequence models can effectively extract features from vessels' historical trajectories and enhance the prediction of remaining sailing time to the destination port.

There are two limitations in the above studies. The first and most significant limitation is that the prediction model highly depends on real-time AIS data of current voyage. The accuracy of prediction degenerates significantly if the AIS data is unavailable ([Chu et al. 2025](#)). It determines that the model above can only be used for the sailing duration prediction task on current segment but not future voyage segments. Besides, the studies above do not make full use of the sailing duration time series on each segment. For each voyage segment, historical sequences of sailing durations involve changing patterns which are useful for long-term forecasting. Explicitly modeling the sequence of sailing duration helps the model to extract inherent features and enhance ETA prediction accuracy.

2.2. Inland ETA Prediction

Inland transportation has some features in common with maritime transportation. Both domains rely on trajectory data sources. In maritime transportation, vessel movements are captured by AIS data, whereas in inland logistics, vehicle trajectories are collected through GPS devices. Similarly, maritime voyage segments between ports correspond to road segments in land traffic networks. ETA in both situations is influenced by congestion factors. In the field of road transportation, researchers have extensively applied temporal forecasting models to capture traffic dynamics and to predict the arrival time of vehicles. Given these similarities, many time series prediction techniques developed for inland ETA can provide methodological insights for maritime applications.

[Liu et al. \(2024\)](#) introduced iTransformer, an inverted attention architecture that treats variables as tokens, enabling the model to learn cross variable dependencies effectively. This design is able to capture relationship of traffic flow dynamic on approaching routes, reporting to deliver strong long-term forecasts on standard benchmarks that include traffic data. [Derrow-Pinion et al. \(2021\)](#) presented a graph neural network (GNN) framework for ETA prediction that has been deployed in Google Maps, yielding substantial accuracy gains over prior production models. The approach partitions the road network into spatially adjacent supersegments and constructs a directed spatiotemporal graph in which nodes represent supersegments and edges encode traffic influence. By learning interactions across neighboring supersegments and capturing network-wide congestion propagation, the method improves robustness under dynamic traffic conditions. [Liu et al. \(2023\)](#) addressed the critical need for quantifying prediction reliability in ride-hailing services by proposing an uncertainty-aware probabilistic deep learning model ProbTTE for travel time prediction. The framework not only generates accurate point estimates but also outputs the parameters of a probability distribution, effectively capturing the inherent variability and uncertainty in urban traffic.

However, there are some gaps between inland transportation and maritime transportation. Firstly, road vehicles must follow predefined links in a road network, so the travel time is largely determined by paths constrained to the road graph. By contrast, maritime voyages are weakly constrained by fixed trajectories and vessels can select among multiple routes. As a result, the sailing time between two ports can vary substantially due to route choice and the differences in nautical distance. Secondly, congestion in inland systems typically happened on the road. In maritime settings, congestion concentrates at ports but not along the voyage segments. Vessels generally adjust speed when approaching the destination port, responding to berth availability and port operations. Thirdly, sailing times are significantly influenced by vessel-specific attributes. This leads to high variance in sailing durations even for vessels departing on the same voyage segment at proximate times, a phenomenon markedly different from the relatively stable travel times observed on road segments.

2.3. Research Gap

In summary, while contemporary maritime ETA prediction literature has achieved significant accuracy, the majority of studies remain confined to estimating the remaining sailing duration of the current segment by leveraging real-time AIS data and immediate vessel states. The heavy reliance on real-time AIS information inherently restricts the predictive horizon and compromises model robustness in scenarios where signals are delayed, absent, or unavailable for future segments. Furthermore, existing methodologies often overlook the intrinsic temporal regularities embedded within historical segment-level sailing duration sequences, which are critical assets for effective long-term forecasting. Given the extended temporal span of future voyage segments, immediate vessel-specific behavior features provide diminishing marginal utility.

To bridge these gaps, this study investigates the task of predicting sailing durations for future voyage segments, a domain that has yet to be explored in depth. We pivot the analytical focus from real-time vessel tracking to modeling the long-range temporal dependencies inherent in segment-level sailing duration time series. Specifically, we propose a transformer-based model designed to extract latent evolutionary patterns from historical sailing records, which are then integrated with port congestion proxies and static vessel characteristics to deliver reliable forecasts across global liner services. To further enhance predictive stability, a multi-task learning strategy is adopted to jointly predict destination port congestion and sailing durations on the voyage segment, thereby capturing the correlated latent signals that govern both sailing behavior and port operational efficiency.

3. Method

3.1. Problem Definition

In contrast to conventional vessel-level next-port ETA prediction, we reformulate the task into a time-series forecasting problem at the voyage segment level. Table 1 shows the segment-level data format of sailing records. Specifically, continuous time is discretized into non-overlapping, fixed-length time windows of duration Δt with integer indexes $t \in \mathbb{Z}_{>0}$. Time window t defines the half-open interval $[(t-1)\Delta t, t\Delta t)$ which guarantees each timestamp belongs to exactly one time window and adjacent time windows share no overlap. Let $\mathcal{P} = \{p^{(1)}, p^{(2)}, \dots, p^{(N)}\}$ with the number of ports N denote the set of ports and $p^{(i)}$ represent the i th port. Let $\mathbf{A} = [a^{(ij)}]$ stand for the adjacency matrix.

$$\mathbf{A}(i, j) = \begin{cases} 1, & \text{if segment from } p^{(i)} \text{ to } p^{(j)} \text{ exists} \\ 0, & \text{otherwise,} \end{cases} \quad \mathbf{A} \in \{0, 1\}^{N \times N}$$

Let $\mathcal{E} = \{e^{(ij)}\}$ denote the set of voyage segments in a maritime liner network, where each segment $e^{(ij)} = (p_i \rightarrow p_j)$ connects two consecutive ports p_i to p_j and $|\mathcal{E}| = K$, where K is the total number

Table 1 An example of sailing record data format on the segment-level view

Segment	Start time	Vessel ID	Sailing time (h)
Hong Kong → Singapore	2021-01-10 06:00:00	10254	120.00
Hong Kong → Singapore	2021-01-11 12:00:00	10069	105.00
Hong Kong → Singapore	2021-01-12 18:00:00	10236	95.00

of voyage segments. For each segment $e^{(ij)}$, historical sequence of sailing durations is collected as $\mathbf{Y}_{T-L:T}^{(ij)} = [\mathbf{y}_{T-L}^{(ij)}, \mathbf{y}_{T-(L-1)}^{(ij)}, \dots, \mathbf{y}_{T-1}^{(ij)}]$ indexed by departure time windows t , where T denotes the time window index of timestamp to make predictions, L denotes the length of lookback period, and $\mathbf{y}_t^{(ij)}$ represents the sailing duration on segment $e^{(ij)}$ with the departure in time window t . In addition, both time-varying covariates and static features are incorporated to enhance the forecasting accuracy. Some covariates can only be observed up to the time window T , such as historical port congestion levels. These covariates are denoted as $\mathbf{X}_{T-L:T}^{(ij)} = [\mathbf{x}_{T-L}^{(ij)}, \mathbf{x}_{T-(L-1)}^{(ij)}, \dots, \mathbf{x}_{T-1}^{(ij)}]$, where $\mathbf{x}_t^{(ij)}$ represents the observable covariates on segment $e^{(ij)}$ in time window t before time window T . Other features can be known for both past and future periods, for instance, weekday of the departure time window and static vessel characteristics. These variables are denoted as $\mathbf{S}_{T-L:T+H}^{(ij)} = [\mathbf{s}_{T-L}^{(ij)}, \mathbf{s}_{T-(L-1)}^{(ij)}, \dots, \mathbf{s}_T^{(ij)}, \mathbf{s}_{T+1}^{(ij)}, \dots, \mathbf{s}_{T+(H-1)}^{(ij)}]$ where H represents the length of forecasting horizon. $\mathbf{s}_t^{(ij)}$ represents these feature variables on segment $e^{(ij)}$ in time window t . By jointly modeling $\mathbf{Y}_{T-L:T}^{(ij)}$, $\mathbf{X}_{T-L:T}^{(ij)}$ and $\mathbf{S}_{T-L:T+H}^{(ij)}$, the predictive framework can leverage historical dynamic information while conditioning on known future static features, therefore improving long-term prediction accuracy and stability.

The objective of the framework is to predict the sailing durations associated with the congestion levels in destination ports for future horizons H ,

$$\hat{Y}_{T:T+H}^{(ij)} = [\hat{y}_T^{(ij)}, \hat{y}_{T+1}^{(ij)}, \dots, \hat{y}_{T+(H-1)}^{(ij)}],$$

$$\hat{X}_{T:T+H}^{(ij)} = [\hat{x}_T^{(ij)}, \hat{x}_{T+1}^{(ij)}, \dots, \hat{x}_{T+(H-1)}^{(ij)}],$$

where $\hat{y}_t^{(ij)}$ is the predicted sailing duration of segment e_{ij} at future time window t and $\hat{x}_t^{(ij)}$ is the congestion level in destination port of segment e_{ij} at future time window t . The model thus learns a mapping

$$f : (\mathbf{Y}_{T-L:T}^{(ij)}, \mathbf{X}_{T-L:T}^{(ij)}, \mathbf{S}_{T-L:T+H}^{(ij)}) \mapsto (\hat{Y}_{T:T+H}^{(ij)}, \hat{X}_{T:T+H}^{(ij)}), \text{ for } e^{(ij)} \in \mathcal{E}$$

This formulation allows the model to provide segment-level sailing time forecasting over the future horizons. Once the predicted sailing time is obtained for a given segment e_{ij} over the horizon from time window T to $T + (H - 1)$, the estimated voyage time of a particular vessel on segment e_{ij} can be derived by aligning the departure timestamp with the corresponding time window. In this way, the framework changes the view from vessel-level to segment-level, enabling one model to be used for different vessels, achieving more robust and stable predictions.

3.2. Data Preprocessing

To construct such model, sailing durations of each voyage segment and port congestion levels are essential features. Therefore, it is necessary to first establish a data preprocessing pipeline that transforms raw data into structured voyage records dataset and port vessel count dataset, serving for further utilization. The raw data contains AIS data, port geofence data and static vessel information. The basic items of raw data above would be described in Appendix A.

It's important to give an accurate and objective definition for the sailing duration because it serves as the target label for model prediction. As illustrated in Figure 2, the general process of vessel departure and arrival involves several major spatial zones, including the departure port pilotage area, open sea area, destination port anchorage area, destination port pilotage area and destination port berth. Since the sailing duration is intended to characterize vessels' navigation behavior in open sea area rather than within near-port waters, the sailing duration is defined as the time elapsed between leaving the departure port pilotage area and arriving at the destination port anchorage area.

Based on this definition, the port geofence data can be used to segment vessel AIS trajectories into separate voyages, allowing each trajectory segment to be aggregated into a structured voyage record. Specifically, for each vessel's complete AIS data, the vessel's latitude-longitude coordinates are first intersected with the berth boundaries contained in the port geofence dataset to identify the departure and destination ports for each voyage. For any two consecutive berthing events, the AIS trajectories are further intersected with the pilotage boundary of the departure port and the anchorage boundary of the destination port. The last AIS point within the departure port's pilotage area is regarded as the departure mark, and the first AIS point within the destination port's anchorage area is regarded as the arrival mark. The time difference between these two points is recorded as the sailing duration of the voyage. Finally, by matching the vessel's IMO identifier with the static vessel information, the corresponding vessel characteristics can be attached to each voyage record. Subsequently, origin voyage records are synchronized onto the discrete timeline by aligning each voyage's actual departure timestamp to its unique time window $t = [(t - 1)\Delta t, t\Delta t]$. In this way, regularized voyage record dataset is constructed.

On this basis, constructing the port vessel count dataset becomes relatively straightforward. Specifically, assuming that the initial number of vessels in each port is zero, the voyage record dataset which records voyage segments, vessel departure time and sailing durations can be used to calculate the number of vessels arriving at and departing from each port within every time window t , therefore deriving the relative vessel count for each port over time.

Through this pipeline, a structured dataset of regularized voyage records and port vessel count can be obtained for subsequent analysis and modeling.

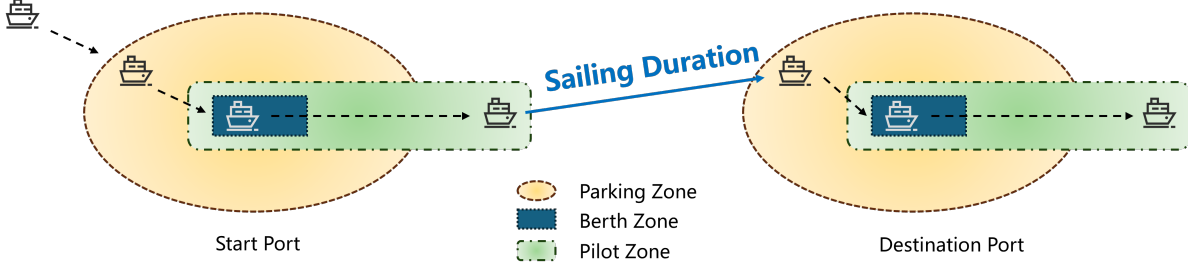


Figure 2 The schematic diagram of vessel departure and arrival process.

3.3. Feature Engineering

Selecting appropriate and informative features is crucial for improving the predictive accuracy of the model. For the task of long-term sailing duration prediction on voyage segments, three categories of features are primarily considered: temporal features, vessel features and segment features. Table 2 summarizes the selected input features. The details of each feature group are described in the following subsections.

Table 2 Summary of input features for voyage segment duration prediction.

Feature Name	Category	Notation	Time Span
Historical sailing duration sequence	Temporal	$\mathbf{Y}_t^{(ij)} = \{y_t^{(ij)}\}$	$t \in [T-L, T-1]$
Historical vessel count sequence at destination port	Temporal	$\mathbf{X}_t^{(ij)} = \{x_t^{(j)}\}$	$t \in [T-L, T-1]$
Time window identifier	Temporal	$\mathbf{I}_t = \{g_t, r_t\}$	$t \in [T-L, T+(H-1)]$
Vessel static characteristics	Vessel	$\mathbf{V}_t^{(ij)} = \{l_t^{(ij)}, w_t^{(ij)}, u_t^{(ij)}, c_t^{(ij)}\}$	$t \in [T-L, T+(H-1)]$
Segment identifier	Segment	$\mathbf{R}_t^{(ij)} = \{p^{(i)}, p^{(j)}, m_t^{(ij)}\}$	$t \in [T-L, T+(H-1)]$

3.3.1. Temporal Features Temporal features are designed to capture the dynamic changing pattern of both segment-level sailing durations and port congestion over time. In the study, two major time dependent sequential variables are employed. The first is the historical time series of sailing durations for each voyage segment. This variable reflects the temporal continuity and periodic variation of sailing efficiency, which may be influenced by seasonal patterns. By modeling the sequential correlation among past sailing duration sequences, the model can learn long-term temporal dependencies and better predict future voyage times. The feature of sailing durations for each voyage segment can be denoted as $y_t^{(ij)}$, representing the sailing duration of segment $p_i \rightarrow p_j$ with departure timestamp in time window t . The sequence $[y_{T-L}^{(ij)}, y_{T-(L-1)}^{(ij)}, \dots, y_{T-1}^{(ij)}]$ constructs the sequential feature $\mathbf{Y}_{T-L:T}^{(ij)}$ defined in Section 3.1.

The second sequential temporal feature is the historical time series of the vessel count at the destination port. This feature serves as a proxy for port congestion, representing the operational

load of the destination port at each time window. The congestion level directly affects the decision of the captain. Captains tend to lower down the speed of the vessel to save the energy if they are informed the congestion of the destination port because they have to wait in queue to get the service. Cooperating with the time series allows the model to capture not only seasonal patterns within sailing durations sequences but also external factors caused by port operations. Together, these temporal features enable the model to effectively integrate sequential information and external temporal dependencies for more accurate long-term sailing duration forecasting. The feature of vessel number at the destination port can be denoted as $x_t^{(j)}$, representing the vessel number at the destination port j in time window t . The sequence $[x_{T-L}^{(j)}, x_{T-(L-1)}^{(j)}, \dots, x_{T-1}^{(j)}]$ constructs the sequential feature $\mathbf{X}_{T-L:T}^{(ij)}$ defined in Section 3.1. $x_t^{(j)}$ is not related to the start port of the segment p_i , so it is indexed with the destination port p_j only.

Beyond the two aforementioned sequential temporal features, the weekday of the departure time window g_t and its positional order index within the day r_t are selected as identifiers for each time window t . Let $\mathbf{I}_t = \{g_t, r_t\}$ denote the identifier of time window t . The sequence $\mathbf{I}_{T-L:T+H} = [\mathbf{I}_{T-L}, \mathbf{I}_{T-(L-1)}, \dots, \mathbf{I}_T, \mathbf{I}_{T+1}, \dots, \mathbf{I}_{T+(H-1)}]$ belongs to the feature $\mathbf{S}_{T-L:T+H}^{(ij)}$ defined in Section 3.1. \mathbf{I}_t only depends on the time window t so that the index for segments is omitted.

3.3.2. Vessel Features Vessel features describe the physical characteristics of containers that may influence their sailing performances. These static attributes remain constant for a given vessel and serve as important features for sailing duration prediction. Key features such as vessel length, vessel width and vessel twenty-foot equivalent unit (TEU) are selected. These features describe the size and capacity of vessels, indicating different voyage patterns. Besides, the carrier of the vessel serves as a significant features. Different carriers prefer different routes even for the same voyage segment. Therefore, the different choices of routes cause that the actual sailing distance becomes different among carriers, resulting in the variance of sailing durations. Vessel features including vessel length, vessel width, vessel TEU, and vessel carriers are be denoted as $\mathbf{V}_t^{(ij)} = \{l_t^{(ij)}, w_t^{(ij)}, u_t^{(ij)}, c_t^{(ij)}\}$, representing the vessel's features $\mathbf{V}_t^{(ij)}$ including vessel length $l_t^{(ij)}$, vessel width $w_t^{(ij)}$, vessel TEU $u_t^{(ij)}$, and vessel carriers $c_t^{(ij)}$ on segment $p_i \rightarrow p_j$ with the departure timestamp in time window t . The sequence $\mathbf{V}_{T-L:T+H}^{(ij)} = [\mathbf{V}_{T-L}^{(ij)}, \mathbf{V}_{T-(L-1)}^{(ij)}, \dots, \mathbf{V}_T^{(ij)}, \mathbf{V}_{T+1}^{(ij)}, \dots, \mathbf{V}_{T+(H-1)}^{(ij)}]$ belongs to the feature $\mathbf{S}_{T-L:T+H}^{(ij)}$ defined in Section 3.1.

3.3.3. Segment Features Different segments have their inherent characteristics, which determine the variability of sailing durations and their sensitivity to external conditions. The changing pattern of voyage time and its correlation with port congestion may vary significantly across different segments. To capture such heterogeneity, several segment-level features are incorporated

into the model. The start port and destination port serve as a unique identifier of the segment. Besides, the arriving terminal of destination port is selected, considering different congestion levels of different terminals in the same port. Segment features including start port, destination port and destination terminal are denoted as $\mathbf{R}_t^{(ij)} = \{p^{(i)}, p^{(j)}, m_t^{(ij)}\}$, where $\mathbf{R}_t^{(ij)}$ represents the features of segment $p_i \rightarrow p_j$ with departure timestamp in time window t , including start port $p^{(i)}$, destination port $p^{(j)}$ and destination terminal $m_t^{(ij)}$. The sequence $\mathbf{R}_{T-L:T+H}^{(ij)} = [\mathbf{R}_{T-L}^{(ij)}, \mathbf{R}_{T-(L-1)}^{(ij)}, \dots, \mathbf{R}_T^{(ij)}, \mathbf{R}_{T+1}^{(ij)}, \dots, \mathbf{R}_{T+(H-1)}^{(ij)}]$ belongs to the feature $\mathbf{S}_{T-L:T+H}^{(ij)}$ defined in Section 3.1. It's notable that features $p^{(i)}$ and $p^{(j)}$ don't change with the time window t since the start port and destination port keep the same with the selected segment. The feature $m_t^{(ij)}$ is associated with segment $p_i \rightarrow p_j$ and time window t because the choice of destination terminal can vary from different segments and different time windows on the same segment.

3.4. Model Design

The purpose of the proposed model is to accurately predict the sailing duration of each voyage segment in a long term for future-port ETA forecasting by capturing the pattern of sailing duration time series and correlation with exogenous covariates. The overall architecture of proposed model is shown in Figure 3. Formally, the model aims to forecast the sailing duration $\mathbf{Y}_{T:T+H}^{(ij)} = [y_T^{(ij)}, y_{T+1}^{(ij)}, \dots, y_{T+(H-1)}^{(ij)}]$ on segment $p_i \rightarrow p_j$ associated with vessel count $\mathbf{X}_{T:T+H}^{(ij)} = [x_T^{(j)}, x_{T+1}^{(j)}, \dots, x_{T+(H-1)}^{(j)}]$ in destination port p_j for the future H time steps with the given features $\mathbf{Y}_{T-L:T}^{(ij)}$, $\mathbf{X}_{T-L:T}^{(ij)}$ and $\mathbf{S}_{T-L:T+H}^{(ij)} = \{\mathbf{I}_{T-L:T+H}, \mathbf{V}_{T-L:T+H}^{(ij)}, \mathbf{R}_{T-L:T+H}^{(ij)}\}$.

3.4.1. Input Representation For each voyage segment $p_i \rightarrow p_j$, the input features contain two types, continuous features and categorical features. For time windows without observed voyage records, the input features related to sailing records $y_t^{(ij)}$, $\mathbf{V}_t^{(ij)}$ and $m_t^{(ij)}$ are filled with null values. For time windows with multiple observed voyage records, one record is selected in random. Besides, due to the availability of different features, the feature lengths may differ from L (e.g. $\mathbf{X}_{T-L:T}^{(ij)}$) to $L + H$ (e.g. $\mathbf{V}_{T-L:T+H}^{(ij)}$). So, it's important to introduce a module to unify the format of input features and convert the scalar features into vectors.

To address the missing data, zero is padded to the features related to sailing records in time windows with no observation. Besides, since there is no knowledge about sailing durations and vessel count in destination ports in the future, zero padding is also added to these time series features to keep the length the same between different features:

$$\tilde{\mathbf{Y}}_{T-L:T+H}^{(ij)} = [\mathbf{Y}_{T-L:T}^{(ij)} \parallel \mathbf{0}_H], \tilde{\mathbf{X}}_{T-L:T+H}^{(ij)} = [\mathbf{X}_{T-L:T}^{(ij)} \parallel \mathbf{0}_H],$$

where $\mathbf{0}_H$ denotes an H -length zero vector, $\tilde{\mathbf{Y}}_{T-L:T+H}^{(ij)}$ and $\tilde{\mathbf{X}}_{T-L:T+H}^{(ij)}$ represent for the corresponding sequence after padding. For categorical features $\mathbf{R}_t^{(ij)} = \{p^{(i)}, p^{(j)}, m_t^{(ij)}\}$, $\mathbf{I}_t = \{g_t, r_t\}$ and $c_t^{(ij)}$,

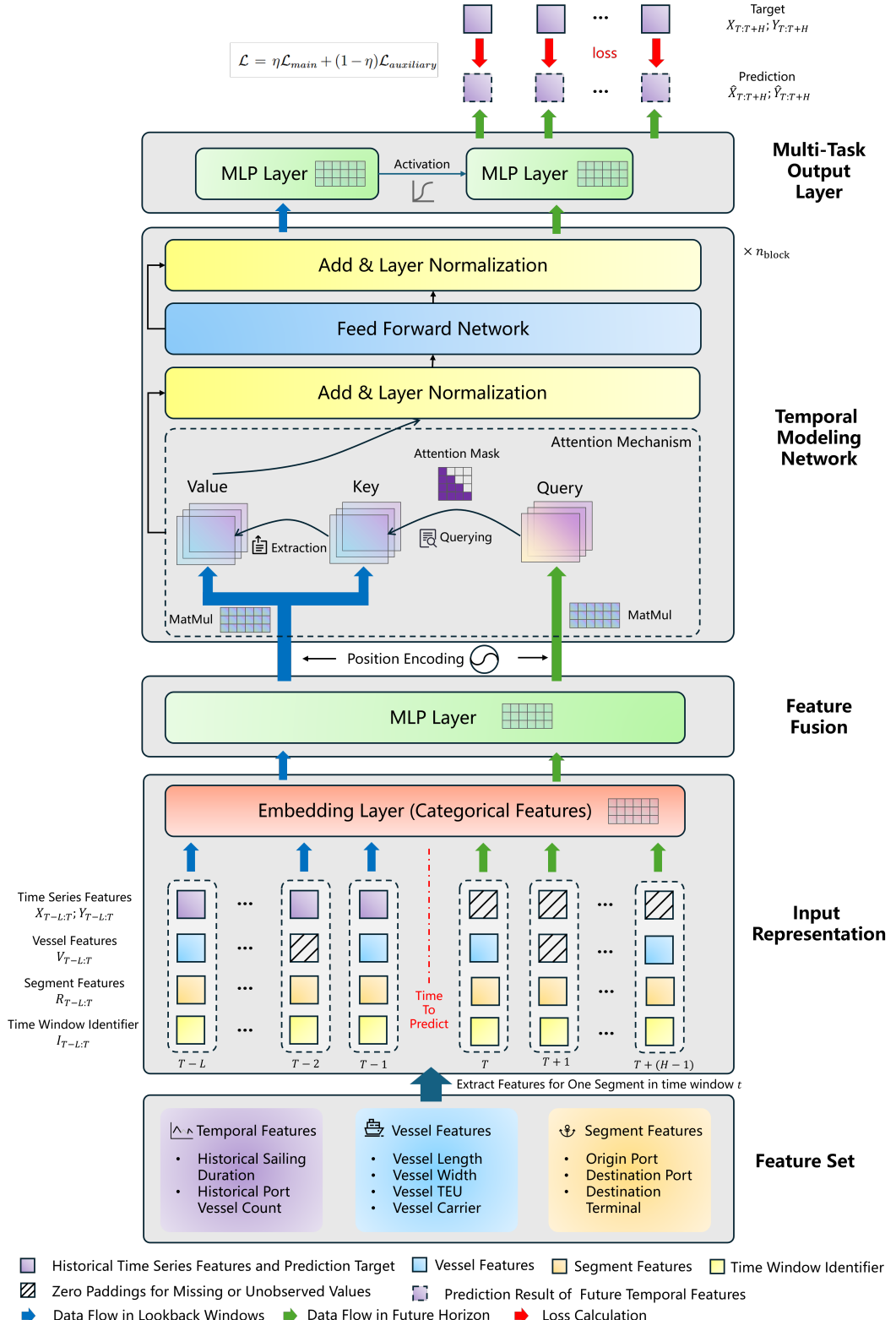


Figure 3 The overall structure of the proposed model.

embedding layers $\mathbf{Emb}(\cdot)$ are designed for each variable to convert it from to one-hot variables into dense vectors $\in \mathbb{R}^{d_{\text{emb}}}$ with trainable parameters:

$$\begin{aligned}\tilde{\mathbf{I}}_{T-L:T+H} &= [\text{Concat}(\mathbf{Emb}_g(g_t), \mathbf{Emb}_r(r_t))]_{t=T-L}^{T+(H-1)}, \\ \tilde{\mathbf{R}}_{T-L:T+H}^{(ij)} &= [\text{Concat}(\mathbf{Emb}_p(p^{(i)}), \mathbf{Emb}_p(p^{(j)}), \mathbf{Emb}_m(m_t^{(ij)}))]_{t=T-L}^{T+(H-1)}, \\ \tilde{\mathbf{V}}_{T-L:T+H}^{(ij)} &= [\text{Concat}(l_t^{(ij)}, w_t^{(ij)}, u_t^{(ij)}, \mathbf{Emb}_c(c_t^{(ij)}))]_{t=T-L}^{T+(H-1)}, \\ \tilde{\mathbf{S}}_{T-L:T+H}^{(ij)} &= \text{Concat}(\tilde{\mathbf{V}}_{T-L:T+H}^{(ij)}, \tilde{\mathbf{R}}_{T-L:T+H}^{(ij)}, \tilde{\mathbf{I}}_{T-L:T+H}).\end{aligned}$$

This embedding scheme converts heterogeneous discrete attributes into a unified, dense representation that preserves categorical semantics while remaining compatible with downstream sequence models. $\tilde{\mathbf{I}}_{T-L:T+H}$, $\tilde{\mathbf{R}}_{T-L:T+H}^{(ij)}$, $\tilde{\mathbf{V}}_{T-L:T+H}^{(ij)}$, $\tilde{\mathbf{S}}_{T-L:T+H}^{(ij)}$ represent the corresponding feature vectors after embedding and $\text{Concat}(\cdot)$ operation combines the feature vectors at each corresponding time window across the different input sequences. To form the final input, the embedding matrix of static features $\tilde{\mathbf{S}}_{T-L:T+H}^{(ij)}$ is concatenated with time series features $\tilde{\mathbf{Y}}_{T-L:T+H}^{(ij)}$ and $\tilde{\mathbf{X}}_{T-L:T+H}^{(ij)}$:

$$\xi_{T-L:T+H}^{(ij)} = \text{Concat}(\tilde{\mathbf{Y}}_{T-L:T+H}^{(ij)}, \tilde{\mathbf{X}}_{T-L:T+H}^{(ij)}, \tilde{\mathbf{S}}_{T-L:T+H}^{(ij)}),$$

where $\xi_{T-L:T+H}^{(ij)} \in \mathbb{R}^{(L+H) \times (6d_{\text{emb}}+5)}$ denotes the final input matrix.

3.4.2. Feature Fusion Before feeding the inputs into the temporal modeling network, early feature fusion is performed to jointly encode different features including sailing durations, vessel count in destination port, and static features of vessels and segments within each time window. Early feature fusion is necessary for the extraction of cross features between sailing durations and other dynamic or static features, which can explain for the variation of sailing durations.

Concretely, let $\xi_t^{(ij)}$ obtained from Section 3.4.1 denote the input vector in time window t for segment $p_i \rightarrow p_j$. One-layer linear transformation is used to obtain the feature fusion representation:

$$\mathbf{h}_t^{(ij)} = \xi_t^{(ij)} \mathbf{W}_1 + \mathbf{b}_1,$$

where $\mathbf{W}_1 \in \mathbb{R}^{(6d_{\text{emb}}+5) \times d_{\text{model}}}$ is the learnable transformation matrix and $\mathbf{b}_1 \in \mathbb{R}^{d_{\text{model}}}$ serves as the bias vector. $\mathbf{h}_t^{(ij)}$ becomes the input to the downstream temporal modeling network.

3.4.3. Temporal Modeling Network To capture and infer dependencies across time windows, a transformer-based network is employed to model the temporal dynamics of the voyage segment's sailing duration. Absolute positional encoding (PE_t) is added to the hidden vector $\mathbf{h}_t^{(ij)}$:

$$\begin{aligned}\text{PE}_t(2i) &= \sin(t \omega_i), & \text{PE}_t(2i+1) &= \cos(t \omega_i), & \omega_i &= 1000^{-\frac{2i}{d_{\text{model}}}}, \\ \tilde{\mathbf{h}}_t^{(ij)} &= \mathbf{h}_t^{(ij)} + \text{PE}_t,\end{aligned}$$

where hidden vectors in different time windows is assigned with a unique mark to indicate its position. $\tilde{\mathbf{h}}_t^{(ij)}$ becomes the hidden vector with positional mark.

The attention mechanism forms the core computational unit of the transformer block (Vaswani et al. (2023)), enabling the model to dynamically weigh and aggregate relevant historical context when making predictions for any given time window. As illustrated in Figure 4, for a target prediction step (e.g., time window $T+1$), each hidden vector $\tilde{\mathbf{h}}_t^{(ij)}$ is linearly projected into three distinct vectors: a query $\mathbf{q}_t^{(ij)}$, a key $\mathbf{k}_t^{(ij)}$, and a value $\mathbf{v}_t^{(ij)}$. The query for the current step is compared with all historical keys via scaled dot-product operations to compute a set of attention weights. These weights determine the relevance of each historical time step to the current prediction. The final contextual representation for the step is then obtained as a weighted sum of the corresponding value vectors. To capture diverse temporal dependencies, multi-head attention is employed. Specifically, multiple sets of query, key, and value projections are learned in parallel, each operating in a reduced dimensional subspace. This allows the network to jointly attend to information from different representation subspaces. Formally, let $\tilde{\mathbf{H}}^{(ij)} = [\tilde{\mathbf{h}}_t^{(ij)}]_{t=T-L}^{T+(H-1)}$, the temporal modeling network follows the equations below:

$$\mathbf{Q}_h^{(ij)} = \tilde{\mathbf{H}}^{(ij)} \mathbf{W}_h^Q, \quad \mathbf{K}_h^{(ij)} = \tilde{\mathbf{H}}^{(ij)} \mathbf{W}_h^K, \quad \mathbf{V}_h^{(ij)} = \tilde{\mathbf{H}}^{(ij)} \mathbf{W}_h^V, \quad h = 1, \dots, n_{\text{head}}$$

$$\mathbf{A}_h^{(ij)} = \frac{\mathbf{Q}_h^{(ij)} \mathbf{K}_h^{(ij)\top}}{\sqrt{d_{\text{model}}}} \odot \text{AttMask} + (1 - \text{AttMask}) \cdot (-\infty), \quad \boldsymbol{\alpha}_h^{(ij)} = \text{Softmax}(\mathbf{A}_h^{(ij)})$$

$$\mathbf{Z}_h^{(ij)} = \boldsymbol{\alpha}_h^{(ij)} \mathbf{V}_h^{(ij)}, \quad \mathbf{Z}^{(ij)} = \text{Dropout} \left(\text{Concat}(\mathbf{Z}_1^{(ij)}, \dots, \mathbf{Z}_H^{(ij)}) \mathbf{W}^O; p_{\text{att}} \right).$$

$\mathbf{W}_h^Q \in \mathbb{R}^{d_{\text{model}} \times (d_{\text{model}}/n_{\text{head}})}$, $\mathbf{W}_h^K \in \mathbb{R}^{d_{\text{model}} \times (d_{\text{model}}/n_{\text{head}})}$, $\mathbf{W}_h^V \in \mathbb{R}^{d_{\text{model}} \times (d_{\text{model}}/n_{\text{head}})}$, $\mathbf{W}^O \in \mathbb{R}^{d_{\text{model}} \times d_{\text{model}}}$ are learnable parameters. $\mathbf{Q}_h^{(ij)}$, $\mathbf{K}_h^{(ij)}$, $\mathbf{V}_h^{(ij)}$, $\boldsymbol{\alpha}_h^{(ij)}$ represent the query matrix, key matrix, value matrix and the attention matrix of h th head respectively. **AttMask** affecting on the attention matrix \mathbf{A}_h denotes the causal mask to avoid the leak of future information:

$$\text{AttMask}(t, s) = \begin{cases} 1, & s \leq t, \\ 0, & s > t, \end{cases} \quad \text{AttMask} \in \{0, 1\}^{(L+H) \times (L+H)}$$

where **AttMask** is a lower triangular matrix. The $\text{Softmax}(\cdot)$ calculator ensures the summation of attention weights from current step to historical steps is equal to 1. The $\text{Dropout}(\cdot; p_{\text{att}})$ calculator with dropout rate p_{att} is utilized to avoid overfitting. $\mathbf{Z}_h^{(ij)}$ and $\mathbf{Z}^{(ij)}$ are the output of h th attention head and final output of masked multi-head attention mechanism respectively. To ensure training stability and effective gradient flow during backpropagation, residual connections and layer normalization are employed:

$$\tilde{\mathbf{Z}}^{(ij)} = \text{LayerNorm}(\mathbf{Z}^{(ij)} + \tilde{\mathbf{H}}^{(ij)}).$$

The $\text{LayerNorm}(\cdot)$ operator normalizes the vector on each time step and $\tilde{\mathbf{Z}}^{(ij)}$ is the hidden matrix after normalization.

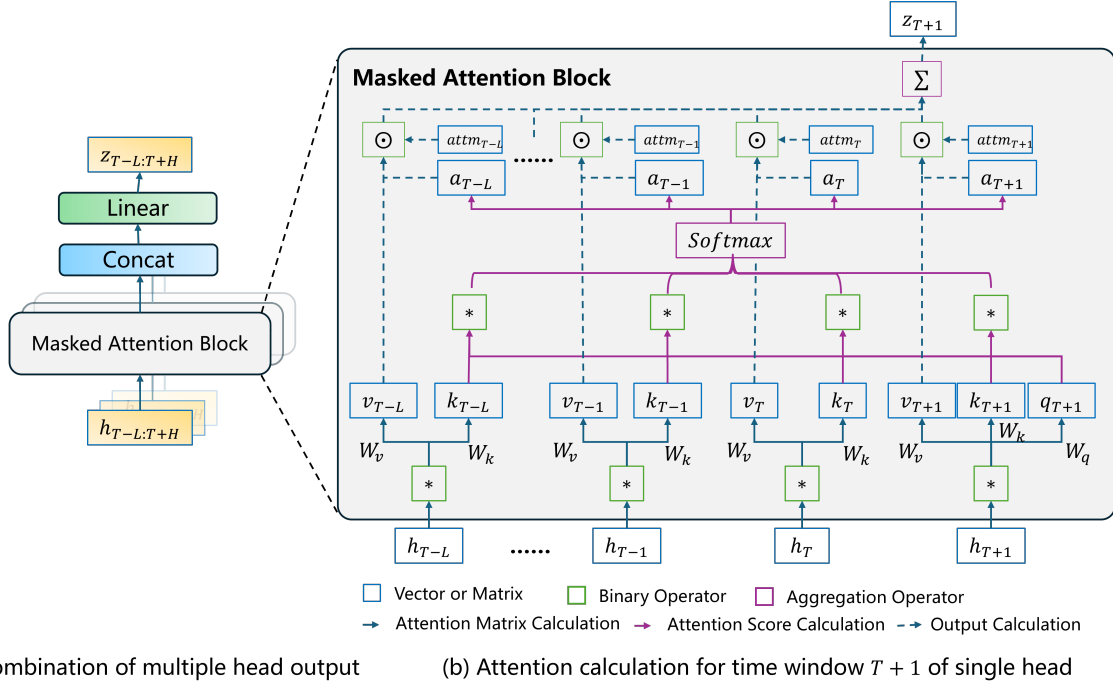


Figure 4 Sketch of masked multi-head attention mechanism.

To further refine these representations and enhance the model's expressive power, a position-wise feed forward network (FFN) is applied to each temporal position independently. This sub-layer consists of two linear transformations with a ReLU activation in between, introducing a non-linear transformation that operates identically on each time step.

$$\mathbf{O}^{(ij)} = \text{Dropout}(\text{ReLU}(\tilde{\mathbf{Z}}^{(ij)} \mathbf{W}_2 + \mathbf{b}_2); p_{\text{ffn}}) \mathbf{W}_3 + \mathbf{b}_3$$

$$\tilde{\mathbf{O}}^{(ij)} = \text{LayerNorm}(\mathbf{O}^{(ij)} + \tilde{\mathbf{Z}}^{(ij)}).$$

$\mathbf{W}_2 \in \mathbb{R}^{d_{\text{model}} \times 4d_{\text{model}}}$, $\mathbf{W}_3 \in \mathbb{R}^{4d_{\text{model}} \times d_{\text{model}}}$, $\mathbf{b}_2 \in \mathbb{R}^{4d_{\text{model}}}$, $\mathbf{b}_3 \in \mathbb{R}^{d_{\text{model}}}$ are learnable transformation matrix and biases respectively. Dropout mechanism with rate p_{ffn} is also employed to avoid overfitting. $\tilde{\mathbf{O}}^{(ij)}$ denotes the output of the FFN block. A residual connection followed by layer normalization is employed to stabilize and accelerate the training process.

The whole operation above in Section 3.4.3 is defined as a Temporal Modeling Network Block (TMNBlock). The block can be built deeper to integrate hidden features:

$$\tilde{\mathbf{O}}^{(ij)} = \text{TMNBlock}^{n_{\text{block}}}(h^{(ij)})$$

where n_{block} denotes the number of stacking TMNBlocks.

3.4.4. Multi-Task Output Layer The output layer converts the hidden matrix $\tilde{\mathbf{O}}^{(ij)}$ into the two final output vectors: sailing durations and vessel count in destination port in the future H time steps. A 2-layer MLP is used in this part:

$$(\hat{\mathbf{Y}}_{T:T+H}^{(ij)}, \hat{\mathbf{X}}_{T:T+H}^{(ij)}) = [\text{ReLU}(\tilde{\mathbf{O}}^{(ij)} \mathbf{W}_4 + \mathbf{b}_4) \mathbf{W}_5 + \mathbf{b}_5]_{T:T+H}.$$

$\mathbf{W}_4 \in \mathbb{R}^{d_{\text{model}} \times d_{\text{temp}}}$, $\mathbf{W}_5 \in \mathbb{R}^{d_{\text{temp}} \times 2}$, $\mathbf{b}_4 \in \mathbb{R}^{d_{\text{temp}}}$, $\mathbf{b}_5 \in \mathbb{R}^2$ are learnable transformation matrix and biases respectively and d_{temp} is the intermediate dimension. As for the final output of the model, only the latest H steps of $\hat{\mathbf{Y}}^{(ij)}$ and $\hat{\mathbf{X}}^{(ij)}$ are selected to calculate for the loss on segment $p_i \rightarrow p_j$. Besides, the mask $M_{T:T+H}^{(ij)}$ is constructed to avoid the loss calculation on missing values of sailing durations:

$$\mathbf{M}_t^{(ij)} = \begin{cases} 1, & y_t^{(ij)} > 0, \\ 0, & \text{otherwise,} \end{cases}$$

where $y_t^{(ij)}$ denotes the real sailing duration with departure timestamp in time window t .

The loss function for the main task of sailing time prediction integrates mean absolute error (MAE) and mean absolute percentage error (MAPE) because both absolute and relative deviations are important. A scalar $\beta \in [0, 1]$ balances the two terms. Define the masked absolute error for segment $p_i \rightarrow p_j$ in time window t as

$$e_t^{(ij)} = \mathbf{M}_t^{(ij)} |y_t^{(ij)} - \hat{y}_t^{(ij)}|.$$

The masked MAE and MAPE over the forecasting horizon H are

$$\begin{aligned} \text{MAE}_T^{(ij)} &= \frac{\sum_{t=T}^{T+(H-1)} e_t^{(ij)}}{H}, \\ \text{MAPE}_T^{(ij)} &= \frac{\sum_{t=T}^{T+(H-1)} \mathbf{M}_t^{(ij)} \frac{|y_t^{(ij)} - \hat{y}_t^{(ij)}|}{y_t^{(ij)}}}{H}. \end{aligned}$$

The total loss for main task on segment $p_i \rightarrow p_j$ is

$$\mathcal{L}_{T,\text{main}}^{(ij)} = \beta \text{MAE}_T^{(ij)} + (1 - \beta) \text{MAPE}_T^{(ij)}.$$

For the auxiliary task of destination port number prediction on segment $p_i \rightarrow p_j$, mean absolute error is adopted:

$$\mathcal{L}_{T,\text{auxiliary}}^{(ij)} = \frac{\sum_{t=T}^{T+(H-1)} |x_t^{(ij)} - \hat{x}_t^{(ij)}|}{H}.$$

The total loss on segment $p_i \rightarrow p_j$ is a combination of loss for main task and auxiliary task. To keep the model concentrating on the main task, the main loss is set with higher weight:

$$\mathcal{L}_T^{(ij)} = \eta \mathcal{L}_{T,main}^{(ij)} + (1 - \eta) \mathcal{L}_{T,auxiliary}^{(ij)}.$$

For a mini batch of $|\mathcal{B}|$ samples, the training objective is to minimize the average of per segment loss:

$$\mathcal{L}_{\mathcal{B}} = \frac{1}{|\mathcal{B}|} \sum_{(i,j,T) \in \mathcal{B}} \mathcal{L}_T^{(ij)}.$$

During training, back propagation mechanism is adopted to update all trainable parameters. Because the main and auxiliary tasks share the representation, their gradients jointly act on the shared features, thereby capturing collaborative signals across ports, segments, and time, improving the joint modeling of future sailing durations and destination port vessel count. Note that the mask $\mathbf{M}_t^{(ij)}$ is applied consistently in both the loss and its gradients, so that only observed targets contribute to learning, preventing noise from missing values.

4. Experiment

4.1. Dataset Description

The original datasets used in the experiment include AIS dataset, port geofence dataset and vessel information dataset. The AIS dataset covers the trajectories of vessels in 2021 worldwide with over 200 million data points observed. The port geofence dataset contains regions of thousands of ports worldwide. To make sure only container ship is considered in the experiment, vessel information dataset is utilized to filter the valid IMO of container ships with the type field. Totally, 5008 container ships are selected.

Through the data preprocessing pipeline described in Section 3.2, vessel voyage records dataset and port vessel count dataset can be accessed for the experiment. The field of vessel voyage records dataset is described in Table 3, which contains the sailing start time, the sailing vessel, the sailing voyage and the sailing duration. In the study, segments with counts more than 75 times in 2021 are considered because sparse data makes it difficult to capture the patterns inherent in the data. Totally, 1120 segments and 380 ports are selected, which are shown in Figure 5. Lines stand for voyage records which happened between the two ports in 2021. It can be seen that most segments gather in the west coast of the Pacific and Europe with short to medium sailing distance. The most frequent segment is from Waigaoqiao port to Ningbo Port, with 2310 observations and 5.37 hours as average sailing duration. The selected segments in the experiment cover 10.4% of segments all over the world, including 54.5% sailing records happened in 2021 with 201510 observations. It can be observed that low frequency segments and short distance segments account for the majority. The frequency of segments usually becomes low with the distance of segments growing. As for port vessel count dataset, it includes 380 ports with the number of vessels on each time window t .



Figure 5 Distribution of global ports and shipping lines with different frequency.

Table 3 Fields and descriptions of regularized vessel voyage record dataset.

Column name	Description
time window	Vessel departure time window
IMO	International Maritime Organization number (unique vessel identifier)
width	Vessel width (beam)
length	Vessel length
TEU	Maximum container capacity (Twenty-foot Equivalent Units)
crrName	Carrier company name
startPortName	Departure port name
endPortName	Destination port name
tmnName	Terminal name
ATA	Actual time of arrival
duration	Actual sailing duration

4.2. Experiment Settings

A comprehensive evaluation of the proposed model is conducted. The dataset is divided into training set from January 1st, 2021 to October 31st, 2021 for model training and test set from November 1st, 2021 to December 31st, 2021 according to the time order for model evaluation, avoiding leak of future information and test data. During training, data from September 1st, 2021 to October 31st, 2021 is remained as the validation test to choose the best model. Considering that it's inconvenient for management and updating to train a model for each segments, one model is trained to give predictions for all the segments.

Table 4 shows the hyperparameter settings of the experiment and proposed model. For the model architecture, the embedding dimension for categorical variables d_{emb} is set to 32; the model dimension d_{model} is set to 32; the number of attention head n_{head} is set to 8; the number of TMNblock layers n_{block} is set to 2; the intermediate dimension of multi-task output layer d_{temp} is set to 16. For regularization, dropout rates of the model p_{ffn} , p_{att} are set to 0.1. For optimization and training settings, Adam optimizer is utilized with default parameters; Learning rate is set to $3e^{-3}$ initially and becomes half every 10 epochs; Batch size is 1024 and 30 epochs can be trained at most. For the task settings, each time slot Δt is set to 6 hours with lookback window length L of 168 time windows (42 days) and forecasting horizon H of 84 time windows (21 days). Loss weight of MAE β is set to 0.8, confirming that MAE loss and MAPE loss are comparable. Loss weight for main task η is set to 0.9.

The training, validation and test samples are generated from the vessel voyage records dataset and port vessel count dataset with sliding window mechanism, as shown in Figure 6. The voyage record dataset is ordered by time window for each segment respectively. The window with width $L+H$ slides along the time axis with the step one. The behind L observations serve as the lookback information while the front H observation serves as the forecasting target. A sample is generated with the window sliding one step.

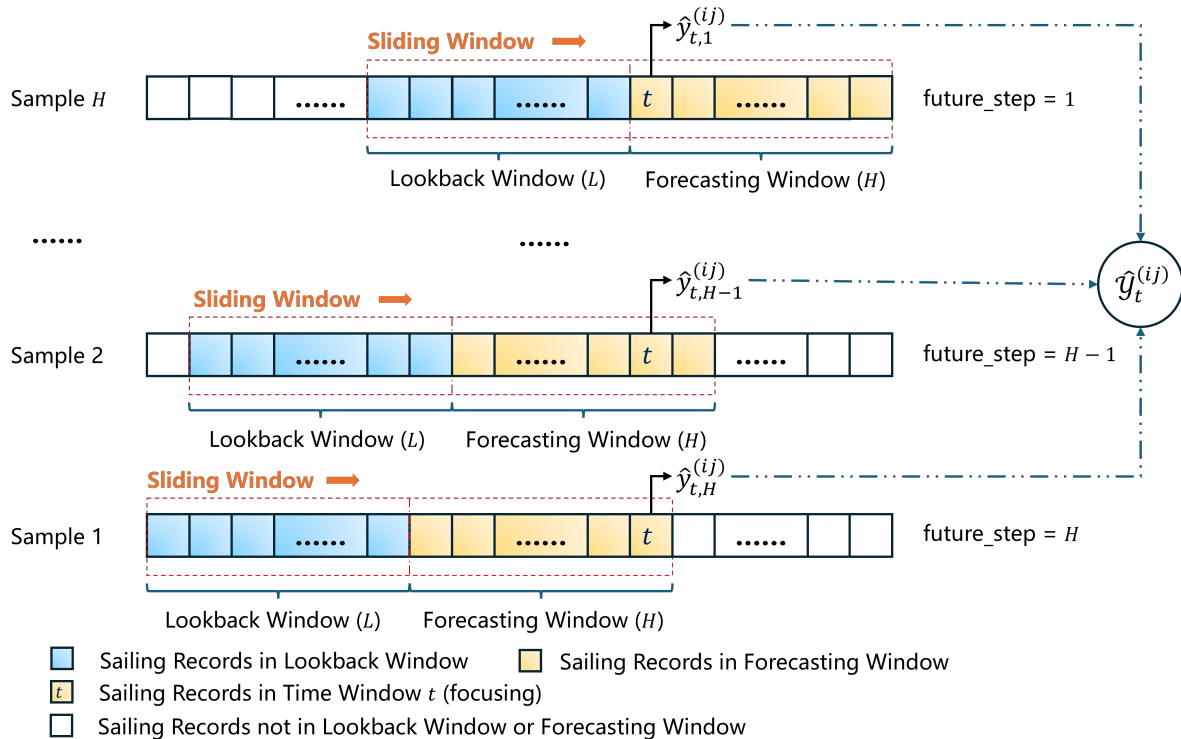


Figure 6 Sliding window mechanism for sample generation.

To better evaluate the performance of the model, several performance metrics are selected. Owing to the sliding window sample generation, for a given ground truth sailing duration $y_t^{(ij)}$, there can be up to H distinct prediction result issued at different future steps for time-series models, which is shown in Figure 6. Let $\hat{y}_{t,k}^{(ij)}$ denote the prediction result for $y_t^{(ij)}$ at future step k and $\hat{\mathcal{Y}}_t^{(ij)} = \{\hat{y}_{t,1}^{(ij)}, \hat{y}_{t,2}^{(ij)}, \dots, \hat{y}_{t,K}^{(ij)}\}$ denote the set of all prediction results for $y_t^{(ij)}$ at different future steps where $K \leq H$. For non-time-series models, the prediction result $\hat{y}_{t,k}^{(ij)}$ at different future steps k keeps the same. Therefore, the prediction error for the sailing record in test dataset is defined as the average over all its available predictions:

$$\text{MAE}_t^{(ij)} = \frac{1}{K} \sum_{k=1}^K |y_t^{(ij)} - \hat{y}_{t,k}^{(ij)}|.$$

$$\text{MAPE}_t^{(ij)} = \frac{1}{K} \sum_{k=1}^K \frac{|y_t^{(ij)} - \hat{y}_{t,k}^{(ij)}|}{y_t^{(ij)}}.$$

Let $v^{(ij)}$ denote the number of sailing records in test dataset on segment $p_i \rightarrow p_j$, the segment-level error is then obtained by averaging the errors of all test records belonging to that segment.

$$\text{MAE}^{(ij)} = \frac{1}{v^{(ij)}} \sum_{y_t^{(ij)} \in \text{TestSet}} \text{MAE}_t^{(ij)}.$$

$$\text{MAPE}^{(ij)} = \frac{1}{v^{(ij)}} \sum_{y_t^{(ij)} \in \text{TestSet}} \text{MAPE}_t^{(ij)}.$$

Given a collection of segments \mathcal{S} , the overall unweighted error is the arithmetic mean of the segment-level errors; the record-weighted error accounts for the number of test samples in each segment:

$$\text{MAE}_{\text{unweighted}}^{\mathcal{S}} = \frac{1}{|\mathcal{S}|} \sum_{e^{(ij)} \in \mathcal{S}} \text{MAE}^{(ij)}, \quad \text{MAE}_{\text{weighted}}^{\mathcal{S}} = \frac{1}{\sum_{e^{(ij)} \in \mathcal{S}} v^{(ij)}} \sum_{e^{(ij)} \in \mathcal{S}} v^{(ij)} \times \text{MAE}^{(ij)},$$

$$\text{MAPE}_{\text{unweighted}}^{\mathcal{S}} = \frac{1}{|\mathcal{S}|} \sum_{e^{(ij)} \in \mathcal{S}} \text{MAPE}^{(ij)}, \quad \text{MAPE}_{\text{weighted}}^{\mathcal{S}} = \frac{1}{\sum_{e^{(ij)} \in \mathcal{S}} v^{(ij)}} \sum_{e^{(ij)} \in \mathcal{S}} v^{(ij)} \times \text{MAPE}^{(ij)},$$

Unless otherwise stated, the MAE and MAPE for the set of voyage segments \mathcal{S} are calculated using the weighted version.

Besides, to analyze the error at different future steps over the forecast horizon, only those records with H available prediction results are considered ($|\hat{\mathcal{Y}}_t^{(ij)}| = H$). The average error at the k th future step ($k = 1, \dots, H$) in forecasting horizon is computed as:

$$\text{MAE}(k) = \frac{1}{\sum_{e^{(ij)} \in \mathcal{E}} v^{(ij)}} \sum_{e^{(ij)} \in \mathcal{E}} \sum_{y_t^{(ij)} \in \text{TestSet}, |\hat{\mathcal{Y}}_t^{(ij)}|=H} |y_t^{(ij)} - \hat{y}_{t,k}^{(ij)}|.$$

$$\text{MAPE}(k) = \frac{1}{\sum_{e^{(ij)} \in \mathcal{E}} v^{(ij)}} \sum_{e^{(ij)} \in \mathcal{E}} \sum_{y_t^{(ij)} \in \text{TestSet}, |\mathcal{Y}_t^{(ij)}|=H} \frac{|y_t^{(ij)} - \hat{y}_{t,k}^{(ij)}|}{y_t^{(ij)}}.$$

This step-wise error profile reveals how predictive accuracy evolves with the future time step increasing.

Table 4 Hyperparameter settings of the experiment and the proposed model.

Category	Hyperparameter	Symbol	Value
Architecture	Embedding dimension	d_{emb}	32
	Model dimension	d_{model}	32
	Number of stacking TMNBlocks	n_{block}	2
	Number of attention heads	n_{head}	8
	Intermediate dimension of output layer	d_{temp}	16
Regularization	Attention dropout rate	p_{att}	0.1
	FFN dropout rate	p_{ffn}	0.1
Optimization & Training	Optimizer	—	Adam
	Learning rate	—	$3e^{-3}$
	LR schedule	—	step
	Batch size	$ \mathcal{B} $	1024
	Max epochs	—	30
Task Setup	Lookback window length	L	168
	Forecast horizon length	H	84
	Time resolution	Δt	6 h
	Loss weight for MAE	β	0.8
	Loss weight for main task	η	0.9

4.3. Result Analysis

To better describe the prediction performance of the proposed model, some baseline models are selected to compare, which have been demonstrated to show great performance from the previous study. Due to baseline models containing time series models and non-time-series models, historical time series are removed from the input and the input data is reconstructed as tabular data for non-time-series models. The baseline models are show as follows:

- **Light gradient boosting machine (LightGBM)** (Lei et al. 2024). A gradient boosting decision tree framework with histogram-based splitting and leaf-wise growth, offering strong accuracy and efficiency on large-scale tabular data.
- **Categorical boosting (CatBoost)**. Gradient boosting that natively handles categorical variables via ordered target statistics and permutation-driven training.

- **Extreme gradient boosting (XGBoost)** (Lei et al. 2024). Regularized gradient boosted trees with shrinkage and column subsampling; a strong tabular model known for robust performance.
- **Stacking model (LightGBM + CatBoost + XGBoost + Linear regression)** (Chu et al. 2025). An ensemble that blends the predictions of three boosted-tree learners using a linear meta-learner.
- **Long short-term memory (LSTM)** (Wenzel et al. 2023). A recurrent neural network with gating mechanisms to capture temporal dependencies and long-range context in sequence data.
- **iTransformer** (Liu et al. (2024)). A transformer-based time-series model that treats variables as tokens and time as channels, enabling global cross-variable attention.

Table 5 shows that the proposed model delivers the best performance under both record-weighted and unweighted evaluations. In the weighted setting, it attains **6.08** h MAE and **18.05%** MAPE. Compared with the best deep learning baseline model LSTM (6.39 h, 18.99%), this constitutes a relative reduction of **4.85%** in MAE and **4.95%** in MAPE. It also outperforms the second best baseline model iTransformer (6.52 h, 20.70%) with a relative reduction of **6.75%** in MAE and **12.80%** in MAPE. Against the strongest tree-based stacking model (6.71 h, 38.38%), the proposed model achieves a much larger relative reduction of **9.39%** in MAE and **52.97%** in MAPE, equivalently, an absolute decrease of **20.33** percentage points in MAPE. Under the unweighted setting, the proposed model achieves **7.23** h MAE and **17.21%** MAPE, surpassing LSTM (7.60 h, 18.24%) with a relative reduction of **4.87%** in MAE and **5.65%** in MAPE, iTransformer (7.77 h, 19.64%) with a relative reduction of **6.95%** in MAE and **12.37%** in MAPE, and the stacking model (7.97 h, 35.15%) with a relative reduction of **9.28%** in MAE and **51.04%** in MAPE. These consistent margins indicate that the proposed architecture of early feature fusion and attention across time windows with auxiliary task learning captures long-horizon temporal patterns more effectively than both recurrent baseline models and non-sequential tree ensembles. iTransformer suffers from the integration of continuous time series features and discrete static features and does not show competitive performances. The large MAPE gaps versus tree methods further suggest improved robustness to scale heterogeneity across segments, and the alignment of gains in weighted and unweighted views implies the benefits are not confined to high frequency segments but generalize across the segment distribution.

Table 6 reports the forecasting results after grouping segments by their *average sailing duration*. The proposed model consistently edges out LSTM and iTransformer on all bins while keeping large margins over tree-based learners. In short segments (< 24 h), it reduces MAE from **2.24** h to **2.21** h (**1.34%** relatively) and MAPE from **23.45%** to **22.51%** (**4.01%** relatively). For segments with average sailing duration 24-72 h, MAE drops from **7.18** h to **6.89** h (**4.04%** relatively) and

Table 5 Performance comparison of models on weighted and unweighted settings.

Model	Weighted setting		Unweighted setting	
	MAE (h)	MAPE	MAE (h)	MAPE
Our Model	6.08	18.05%	7.23	17.21%
LightGBM	7.02	36.88%	8.68	34.26%
CatBoost	8.10	55.87%	9.64	49.60%
XGBoost	7.84	51.82%	9.19	47.66%
Stacking	6.71	38.38%	7.97	35.15%
LSTM	6.39	18.99%	7.60	18.24%
iTransformer	6.52	20.70%	7.77	19.64%

MAPE from **17.08%** to **16.18%** (**5.27%** relatively). For segments with average sailing duration 72-168 h, MAE reduces from **12.72** h to **11.97** h (**5.90%** relatively) with a MAPE reduction from **12.35%** to **11.50%** (**6.88%** relatively). In long segments (168-504 h), the proposed model achieves a reduction of MAE from **27.77** h to **26.92** h (**3.06%** relatively) and MAPE from **11.55%** to **10.94%** (**5.28%** relatively). These gains are most pronounced on medium segments because the record data is dense and regular, allowing the attention layers to capture the changing patterns of time series. The horizon from the predicting time to vessel arrival time at destination port spans from days to several weeks, allowing the auxiliary task to reduce the uncertainty of port congestion level in the future, providing a side signal that sharpens ETA estimation. Tree-based learners remain well behind in every bin, especially on MAPE, reinforcing that explicit temporal modeling is critical. Practically, the result suggests prioritizing the proposed model for medium length segments to improve berth planning and rotations.

Table 7 summarizes the forecasting results after grouping segments by *the number of sailing records* in 2021. The proposed model outperforms LSTM and iTransformer on most of the bins. For segment group with 75-150 records in 2021, it decreases MAE and MAPE by **0.37** h (**4.78%** relatively) and **1.13** percentage points (**6.36%** relatively). For segment group with 151-500 records, MAE reduces by **0.28** h (**4.75%** relatively) and **0.93** percentage points (**4.99%** relatively). For segment group with 501-1000 records, the proposed model achieves a reduction of **0.15** h in MAE (**2.94%** relatively) and **0.85** percentage points in MAPE (**3.52%** relatively). For the highest frequency segment group (1001-5000 sailing records in 2021), the proposed model maintains comparable MAE and MAPE with LSTM and iTransformer (**2.91** h in MAE and **23.78%** in MAPE). Results for tree-based models lag markedly in every group. According to Figure 5 which shows medium-to-high frequency segments correspond to medium-to-short sailing distances, the conclusion from Table 7 can be consistent with that from Table 6. The proposed model performs competitively on medium frequency segments because the dense record enables the attention mechanism

Table 6 Performance comparison of models for different segment groups binned by average sailing duration.

Avg Duration ^a	#Segments ^b	Sum of Records ^c	Model	MAE (h)	MAPE
< 24h	406	86,455	Our Model	2.21	22.51%
			LightGBM	2.85	65.27%
			CatBoost	3.76	107.07%
			XGBoost	3.71	96.81%
			Stacking	2.89	68.37%
			LSTM	2.24	23.45%
			iTransformer	2.32	26.61%
24h-72h	484	81,657	Our Model	6.89	16.18%
			LightGBM	7.29	17.62%
			CatBoost	8.20	20.37%
			XGBoost	8.17	20.99%
			Stacking	7.18	18.33%
			LSTM	7.21	17.08%
			iTransformer	7.45	18.04%
72h-168h	186	28,460	Our Model	11.97	11.50%
			LightGBM	14.09	13.26%
			CatBoost	16.37	15.37%
			XGBoost	15.28	15.42%
			Stacking	12.99	12.73%
			LSTM	12.92	12.63%
			iTransformer	12.72	12.35%
168h-504h	39	4,386	Our Model	26.92	10.94%
			LightGBM	36.17	13.98%
			CatBoost	36.60	14.66%
			XGBoost	32.62	14.11%
			Stacking	30.41	12.70%
			LSTM	27.77	11.55%
			iTransformer	28.86	12.45%

^a Segment classification criteria: range requirements for average sailing durations in 2021.

^b The number of segments in the group.

^c The summation of the number of voyage records in 2021 for all segments in the group.

to capture temporal relationship. Besides, the outperformance on low frequency segments indicates that the learned pattern from other segments may be transferred to low frequency segments.

Figure 7 shows the performance metrics of the proposed model on different future time steps. Due to the sliding window mechanism shown in Figure 6, not all observations have prediction results on all future time steps. For example, the first observation in test set only has prediction results on the first future time step and the last observation only has prediction results on the last future time step. So, only observations with prediction on all future time steps are calculated

Table 7 Performance comparison of models for different segment groups binned by the number of sailing records.

#Records ^a	#Segments ^b	Sum of Records ^c	Model	MAE (h)	MAPE
75–150	678	70,362	Our Model	7.37	16.63%
			LightGBM	9.13	32.08%
			CatBoost	10.29	45.69%
			XGBoost	9.53	42.75%
			Stacking	8.29	32.62%
			LSTM	7.74	17.76%
			iTransformer	7.91	18.52%
151–500	403	99,639	Our Model	5.62	17.71%
			LightGBM	6.08	36.82%
			CatBoost	7.15	55.86%
			XGBoost	7.20	53.98%
			Stacking	6.03	38.59%
			LSTM	5.90	18.64%
			iTransformer	6.06	20.85%
501–1000	26	18,809	Our Model	4.96	23.27%
			LightGBM	5.33	58.57%
			CatBoost	6.11	100.41%
			XGBoost	6.16	80.32%
			Stacking	5.50	62.18%
			LSTM	5.21	24.12%
			iTransformer	5.11	27.10%
1001–5000	9	12,700	Our Model	2.91	23.78%
			LightGBM	3.54	37.16%
			CatBoost	4.60	57.55%
			XGBoost	4.50	49.56%
			Stacking	3.79	39.51%
			LSTM	2.91	23.52%
			iTransformer	3.09	24.91%

^a Segment classification criteria: range requirements for the number of voyage records in 2021.

^b The number of segments in the group.

^c The summation of the number of voyage records in 2021 for all segments in the group.

in this part to make sure the fairness of comparison, which causes a slight difference with overall results in performance metrics. The result indicates that both absolute and relative errors remain in a narrow band across the forecast horizon, suggesting stable long-term performance. The MAE fluctuates gently between **6.40–6.47** h, while MAPE stays within **17.82%–18.00%**. No abrupt spikes or outliers appear in the horizon, showing that the model's error profile is smooth, bounded, and robust over time.

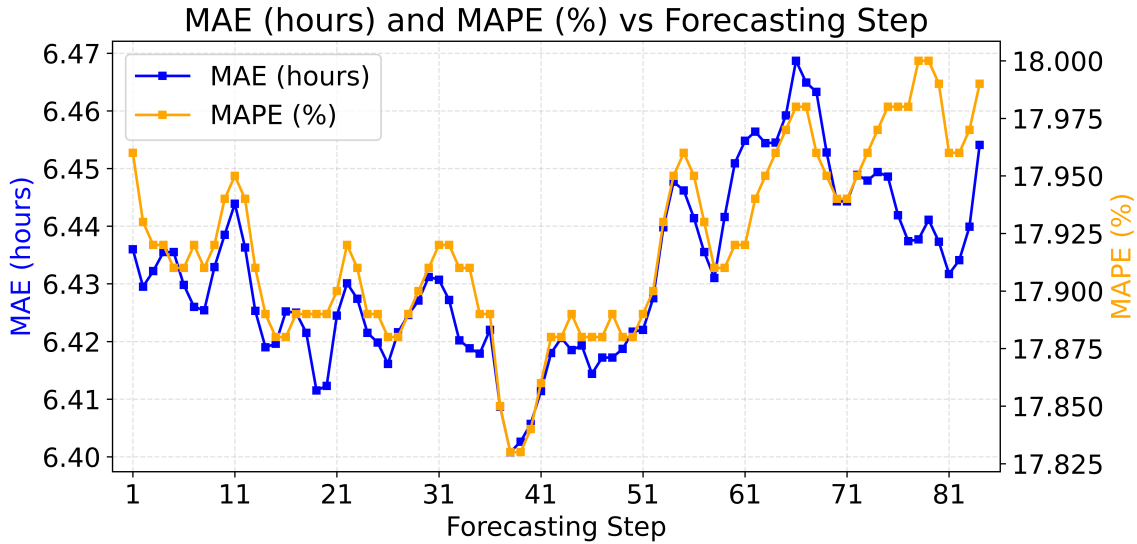


Figure 7 Prediction MAE and MAPE for different future time steps of the proposed model.

4.4. Ablation Study

To verify the effectiveness of input features and time series model design, 4 ablation experiments are conducted. The first one removes the time series features and the model almost falls back to simple MLP network. The second one removes features about vessels. The third one removes features related to the specific segment. The fourth one removes the auxiliary task. For each experiment, a new model is trained from scratch.

Table 8 summarizes the result of ablation study after removing one feature group or auxiliary task at a time. The large degradation arises when time series features or segment features are removed. For the experiment removing time series features, MAE increases by **0.34** h and MAPE by **0.68** percentage points, which hurts the absolute forecasting accuracy significantly. Eliminating segment features also leads to performance degradation, with MAE increasing by **+0.17** h and MAPE increasing by **3.26%** percentage points. This suggests that segment identity, which records segment characteristics such as scale of sailing durations, is particularly important for the relative accuracy of predictions. Removing vessel features leads to **0.18** h increase in MAE and **0.67** percentage points increase in MAPE. If the auxiliary task is removed, MAE increases by **0.06** h and MAPE increases by **0.31** percentage points, which indicates that the task of vessel number prediction at destination ports shares some coordinated signals with the task of sailing duration prediction. Overall, time series features, vessel features, segment features and the auxiliary task design all contribute to the improvement of prediction accuracy. Time series features and segment features contribute the most, followed by the auxiliary task and vessel characteristics.

Table 8 Ablation experiment results of the proposed model.

Setting	Removed features or task	MAE (h)	Δ MAE (h)	MAPE	Δ MAPE
Full model	–	6.08	–	18.05%	–
Ablation 1	Time series features: sailing duration sequence, vessel count sequence	6.42	+0.34	18.73%	+0.68 pp
Ablation 2	Vessel features: width, length, TEU, carrier	6.26	+0.18	18.72%	+0.67 pp
Ablation 3	Segment features: start port, destination port, terminal	6.25	+0.17	21.31%	+3.26 pp
Ablation 4	Auxiliary task	6.14	+0.06	18.36%	+0.31 pp

4.5. Sample Size Sensitivity Analysis

To examine whether the predictive performance of the proposed model is significantly biased toward voyage segments with larger sample sizes, a sensitivity analysis is conducted with respect to the number of observed sailing records per segment. However, since different segments exhibit very different distributions of sailing durations, raw MAE is not directly comparable across segments. To remove the influence of scale, both the ground truth sailing durations and the model prediction within each leg is standardized with Z-Score normalization. Afterwards, MAE with normalized target is computed as segment prediction performance indicators.

Let $d^{(ij)}$ denote the number of sailing records observed for segment $p_i \rightarrow p_j$, and let $\text{MAE}_{\text{norm}}^{(ij)}$ be the corresponding normalized error metrics. The relationship between $d^{(ij)}$ and the indicator is investigated by fitting simple linear regression models.

$$\text{MAE}_{\text{norm}}^{(ij)} = \alpha_{\text{MAE}} + \beta_{\text{MAE}} d^{(ij)} + \varepsilon^{(ij)},$$

Figure 8 shows the relationship concretely.

The estimated slope for normalized MAE is $\beta_{\text{MAE}} \approx -1.33 \times 10^{-4}$ with a 95% confidence interval (CI) $[-2.64 \times 10^{-4}, -2 \times 10^{-6}]$. Although a statistically significant negative trend is detected, its practical magnitude is minimal. Segments with many historical observations and legs with a limited number of observations exhibit comparable normalized MAE, and the variance would be larger for segments with fewer sailing records. The prediction errors remain roughly stable over a wide range of sailing counts, which provides evidence that the model maintains robust generalization capability across voyage legs with different frequency.

4.6. Effect of Time Series Features

Figure 9 compares the prediction result of the proposed model and the LightGBM baseline on the Shekou→Singapore segment over a representative evaluation period. The proposed model, which incorporates historical sailing duration and port vessel count sequences, achieves MAE of **15.97**

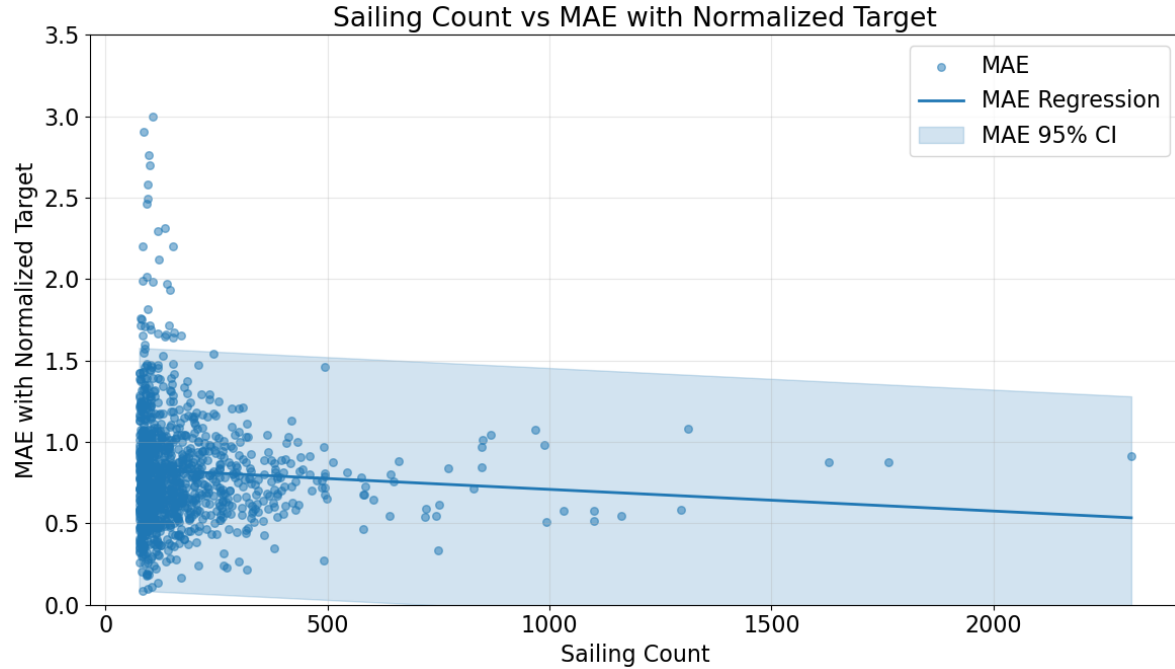


Figure 8 Scatter plot and linear regression line of sailing count vs MAE with normalized target.

h and MAPE of **14.81%**, clearly outperforming the LightGBM baseline whose MAE and MAPE are **19.44 h** and **17.24%**, respectively.

This example illustrates the importance of time series features for accurate sailing duration forecasting on busy liner segments. In the training set, the average sailing duration on this leg is 90.7 hours, whereas during the plotted evaluation window the mean duration rises to 103.3 hours and the current vessel count is clearly high, reflecting the potential congestion around destination port in the near future. By ingesting both historical sailing time sequences and the time series of vessel counts, the attention mechanism can perceive this upward shift in congestion and adjusts its predictions accordingly, with an average forecast of 94.87 hours that better tracks the increasing pattern. In contrast, LightGBM relies mainly on static features and lacks explicit temporal context, so its predictions remain close to the long run mean value (average 85.61 hours), systematically underestimating the actual sailing times. The superior MAE and MAPE of the proposed model stem directly from its ability to exploit dynamic time series features to capture variations in port congestion.

4.7. Interpretation of Attention Mechanism

Figure 10 visualizes the transformer attention from each predictive step (vertical axis) to historical steps (horizontal axis) for the Shekou→Singapore segment. The pattern is sparse and structured rather than average over the history, which means attention mechanism shows the effort. Firstly, a persistent bright band appears from the near future to the most recent history (right down side),

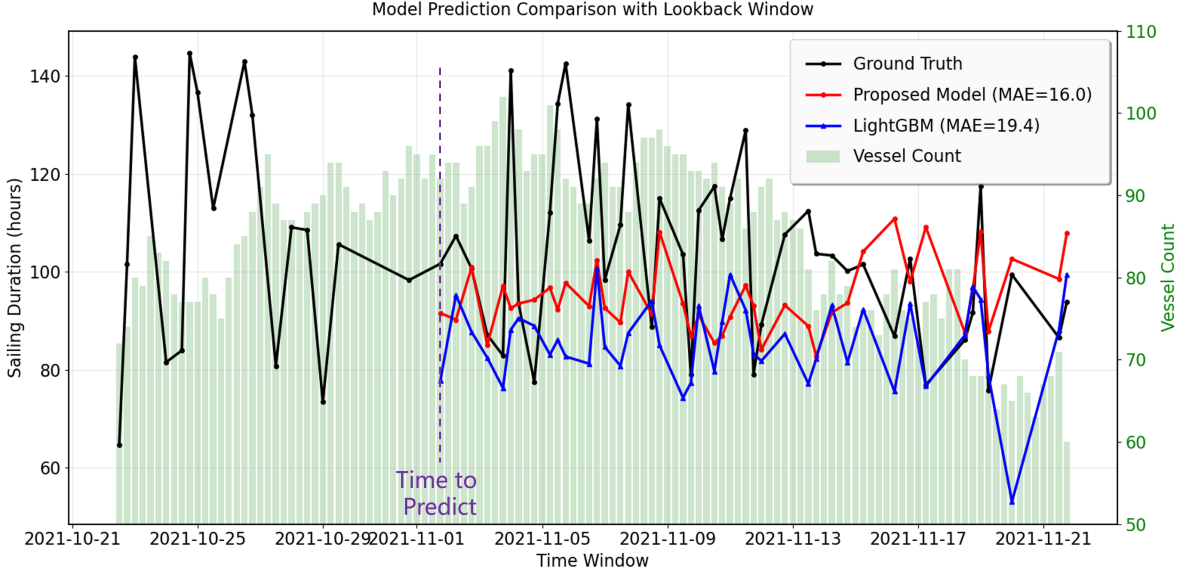


Figure 9 Model prediction comparison for the proposed model and LightGBM (lookback window is truncated).

showing that short lag context remains the primary anchor for the prediction result of near future. Secondly, several vertical stripes at mid-range lags around indices 50-60 attract repeated focus, especially for later forecast steps, indicating that the model reuses specific historical regimes that resemble the current forecast context. Lastly, attention strength intensifies for a narrow cluster of historical positions while remaining low elsewhere, suggesting selective retrieval instead of uniform smoothing. The concentration of weights at a few salient lags helps stabilize long-horizon predictions by anchoring them to representative historical states rather than averaging over heterogeneous periods.

4.8. Hyperparameter Sensitivity

The sensitivity of the proposed model is further investigated with respect to two key hyperparameters: the forecasting horizon and the model capacity. These experiments are designed to evaluate the robustness of the model under different temporal prediction ranges and architectural complexities.

4.8.1. Effect of forecasting horizon In the first experiment, the model architecture and capacity are fixed, while the forecasting horizon H is varied to evaluate the stability of prediction performance across different temporal ranges. Specifically, the forecasting horizon is set to 7 days ($H = 28$), 14 days ($H = 56$), and 21 days ($H = 84$), with all other hyperparameters kept unchanged.

The corresponding MAE and MAPE results are reported in Table 9. Overall, the model maintains stable and comparable performance across different forecasting horizons, indicating strong robustness to the choice of prediction length. In particular, MAE shows only a minimal increase from **6.00** h for $H = 28$ to **6.08** h for $H = 84$, while MAPE remains around **18%** throughout. This

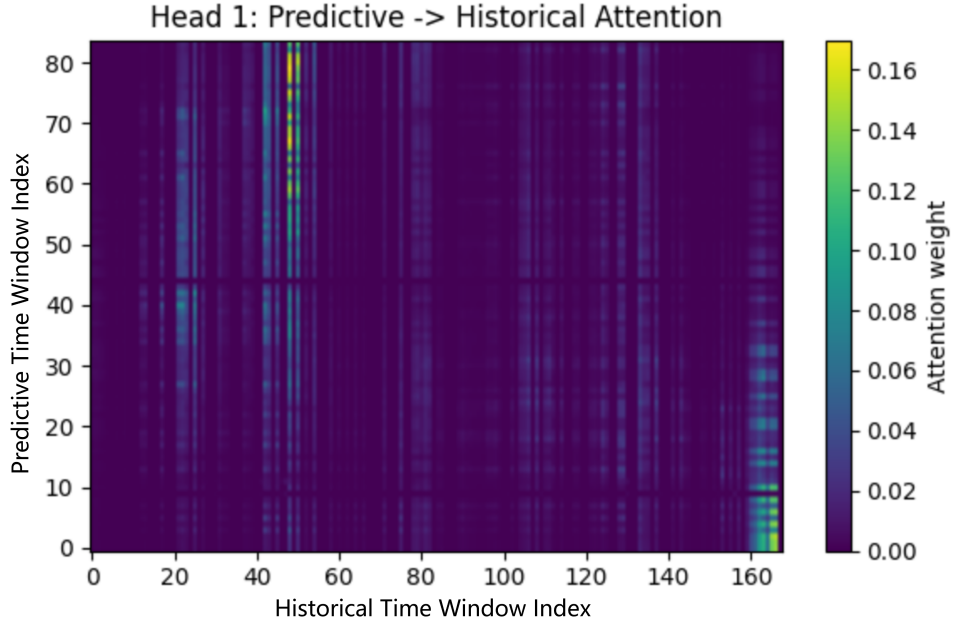


Figure 10 Attention weight heatmap between future and historical steps.

slight variation suggests that extending the horizon does not lead to substantial error accumulation, further confirming the model’s ability to handle long-term dependencies effectively.

This behavior can be attributed to the characteristics of segment-level sailing duration data and the model’s design. The very slight increase in MAE as the forecasting horizon extends from 6.00 h for $H = 28$ to 6.08 h for $H = 84$ suggests that the model is largely robust to the accumulation of uncertainty over longer ranges. While a longer horizon introduces more potential variability, the model’s ability to capture underlying temporal patterns mitigates significant performance degradation. Consequently, the prediction accuracy remains stable across different horizons, demonstrating that the architecture effectively handles both short-term fluctuations and longer-term contextual dependencies.

Table 9 Sensitivity analysis with respect to forecasting horizon (model capacity fixed).

Forecasting Horizon	MAE (h)	MAPE
7 days ($H = 28$)	6.00	17.82%
14 days ($H = 56$)	6.06	18.09%
21 days ($H = 84$)	6.08	18.05%

4.8.2. Effect of model capacity In the second experiment, the forecasting horizon is fixed to 21 days ($H = 84$), while the model capacity is varied by adjusting the number of stacking

TMNBlocks n_{block} , the embedding dimension d_{emb} and the model dimension d_{model} . 8 configurations are considered, covering different combinations of network depth and representation size.

As shown in Table 10, taking both MAE and MAPE into consideration, the model with 2 stacking TMNBlocks, embedding dimension of 32 and model dimension of 32 achieves the best overall performance. When the model capacity is reduced, prediction accuracy deteriorates, suggesting that insufficient capacity limits the model’s ability to capture the diverse temporal patterns in the data. Conversely, increasing the model capacity by enlarging the model dimension also leads to a modest degradation in performance.

These results indicate that the sailing records contain considerable noise, and overly expressive models tend to overfit such noise rather than improving generalization on unseen data. A moderate model capacity therefore provides the most favorable balance, being sufficiently expressive to model heterogeneous segment-level dynamics while remaining robust against noise.

Table 10 Sensitivity analysis with respect to model capacity (forecasting horizon fixed to 21 days).

Model Configuration			Performance Metrics	
#TMNBlocks	Embedding Dimension	Model Dimension	MAE (h)	MAPE
1	16	32	6.15	18.23%
1	16	64	6.14	19.15%
1	32	32	6.15	18.21%
1	32	64	6.15	18.73%
2	16	32	6.17	<u>18.10%</u>
2	16	64	6.07	18.91%
2	32	32	<u>6.08</u>	18.05%
2	32	64	6.17	18.37%

In summary, the hyperparameter sensitivity analysis demonstrates that the proposed model is robust to the choice of forecasting horizon and does not rely on excessive model capacity to achieve strong performance. These properties are particularly important for practical deployment, where stable long-horizon predictions and computational efficiency are critical considerations.

4.9. Case Study: Waigaoqiao Port

In this part, Waigaoqiao port is selected as the destination port for case study. Waigaoqiao (WGQ) is one of Shanghai’s primary gateways linking the Yangtze River Delta to the global liner network. Figure 11 shows the geographical depiction of WGQ. Although ultra-large mainline vessels increasingly berth at Yangshan Deep-Water Port, WGQ remains a critical node that stitches together East-West mainline routes and dense intra-Asia service loops. There are 25 segments in the study with WGQ as destination. Table 11 shows the prediction results on each segments for the proposed model and baseline model. The compared model is set to LSTM as it performs over other baselines.



Figure 11 Waigaoqiao port location overview.

Based on the results, the proposed model attains lower MAE on **17 of 25** segments and lower MAPE on **15 of 25** segments, evidencing both absolute and relative accuracy improvements. The advantages are most pronounced on medium-to-high frequency service lines, where segment-level temporal regularities and port congestion signals are more informative.

5. Conclusion

Persistent uncertainty in vessel sailing durations remains a fundamental bottleneck that degrades maritime schedule reliability and operational efficiency. In particular, the unpredictability of future voyage segments undermines long-term operational planning for downstream ports, leading to inflated costs and the suboptimal allocation of berth, yard, and labor resources. While most existing literature remains confined to estimating the remaining duration of the current segment using real-time AIS, this study addresses the underexplored challenge of forecasting sailing durations for future segments where real-time AIS data is inherently unavailable. We reformulate this problem as a segment-level, time-series forecasting task and bridge the existing research gap through a unified modeling framework.

Specifically, the proposed solution encompasses a robust data processing pipeline that transforms raw AIS, port geofence, and static vessel information into structured voyage records and port vessel count dataset. Building upon this, we introduce a transformer-based architecture featuring causal masking and early feature fusion, which is specifically designed to capture long-range temporal dependencies and historical regularities in the absence of real-time AIS data. To further enhance predictive stability, a multi-task learning strategy is integrated to jointly forecast segment sailing durations and destination port congestion. This approach leverages shared latent signals between port operations and sailing behavior, effectively mitigating the systemic uncertainty associated with future voyage legs.

Empirically, the proposed model consistently outperforms competitive baselines across multiple evaluation protocols. Under record-weighted evaluation, it achieves a mean absolute error (MAE)

Table 11 Segment-level performance comparison between the proposed model and LSTM for Waigaoqiao as the destination port.

Start	Destination	Count ^a	Our model		LSTM	
			MAE (h)	MAPE	MAE (h)	MAPE
Bugo	Waigaoqiao	10	11.33	10.83%	14.23	13.77%
Busan	Waigaoqiao	47	5.41	15.66%	6.21	18.27%
Busan New Port	Waigaoqiao	51	8.22	24.17%	8.11	23.84%
Cat Lai	Waigaoqiao	39	12.15	9.60%	14.52	11.40%
Gwangyang	Waigaoqiao	83	3.55	13.61%	3.71	14.72%
Haiphong	Waigaoqiao	18	9.66	9.73%	10.25	10.35%
Hong Kong	Waigaoqiao	59	7.12	11.94%	7.15	11.98%
Incheon	Waigaoqiao	23	2.67	9.22%	3.08	11.27%
Kaohsiung	Waigaoqiao	59	10.18	20.86%	9.57	20.54%
Keelung	Waigaoqiao	26	4.82	16.40%	5.24	17.06%
Kobe	Waigaoqiao	51	7.79	12.51%	8.81	13.90%
Laem Chabang	Waigaoqiao	7	9.46	6.54%	7.48	5.16%
Moji	Waigaoqiao	24	6.34	16.86%	7.43	20.84%
Nagoya	Waigaoqiao	35	5.61	9.22%	6.04	10.4%
Ningbo	Waigaoqiao	137	1.92	32.64%	2.05	35.34%
Port Klang	Waigaoqiao	16	13.46	9.16%	15.41	9.87%
Qingdao	Waigaoqiao	106	5.18	20.07%	4.67	18.73%
Shimizu	Waigaoqiao	19	4.34	7.66%	4.44	7.86%
Singapore	Waigaoqiao	27	14.22	10.24%	12.79	8.82%
Taichung	Waigaoqiao	16	5.13	14.59%	4.23	12.51%
Tokuyama	Waigaoqiao	14	3.03	10.37%	4.24	14.09%
Tokyo	Waigaoqiao	37	5.78	9.93%	5.73	9.66%
Xiamen	Waigaoqiao	25	6.22	16.07%	8.01	19.50%
Yokohama	Waigaoqiao	51	6.92	10.23%	6.71	9.79%
Zhoushan	Waigaoqiao	25	4.38	27.98%	4.42	27.60%

^a The number of voyage records on the specific segment in test dataset.

of **6.08** h and a MAPE of **18.05%**, improving over the state-of-the-art LSTM by 4.85% and 4.95% relatively, iTransformer by 6.75% and 12.80% relatively. Under the unweighted protocol, it reaches an MAE of **7.23** h and a MAPE of **17.21%**, with respective gains of 4.87% and 5.65% over baseline models relatively. The technical advantage over iTransformer is primarily attributed to the early fusion of heterogeneous signals before temporal decoding, which enables richer cross-feature interactions aligned to each time window and allows the causal decoder to attend over a joint representation. This yields lower errors especially on medium sailing duration segments and medium frequency segments. Furthermore, the model demonstrates a clear superiority over tree-based methods (e.g., LightGBM) by explicitly modeling segment-level historical temporal dynamics that flattened tabular snapshots cannot capture. These design choices result in improved accuracy

for 60.63% of segments in terms of MAE and 66.25% in terms of MAPE. Overall, this study provides a reliable decision-support framework that facilitates long-horizon planning and protects the integrity of transshipment chains across global liner services.

While this study establishes a robust framework for segment-level sailing duration prediction, several avenues remain for future exploration to enhance model reliability and operational depth. First, future research could focus on uncertainty quantification. Implementing probabilistic forecasting techniques such as quantile regression or diffusion-based models would produce calibrated interval predictions, allowing carriers to better manage planning risks (Lee et al. 2021; Wenzhe et al. 2025). This could be further enriched by integrating dynamic environmental variables, including meteorological and oceanographic data, to enhance robustness under extreme conditions.

Second, the current framework could be extended to capture spatiotemporal dependencies across the global maritime network. Utilizing graph neural networks (GNNs) over port-segment graphs would enable the modeling of systemic congestion propagation and inter-route dependencies. Furthermore, incorporating latent route-choice modules could help account for unobserved path heterogeneity across different carrier preferences. Finally, improving model generalization and operational utility is critical. Leveraging transfer learning or continual learning techniques would better support low-frequency segments with sparse historical data (Miao et al. 2024; Yuan et al. 2024). Expanding the multi-task framework to predict additional port-level operations, such as turnaround time and queue length, would also provide a more holistic decision-support tool for synchronized liner service coordination.

Acknowledgments

The acknowledgements section will be completed after the peer-review process.

Declaration of generative AI and AI-assisted technologies in the writing process

During the preparation of this work the authors used ChatGPT 5.2 in order to improve language and help write L^AT_EX. After using this tool, the authors reviewed and edited the content as needed and take full responsibility for the content of the publication.

Appendix.

A. Raw Dataset Description

AIS data, port geofence data and static vessel information serve as the raw dataset in Section 3.2.

Automatic identification system (AIS) data refers to the dynamic and static information of vessels obtained through the shipborne AIS device. The system periodically broadcasts information such as vessel name,

Table 12 AIS data fields and descriptions

Column name	Description
createTime	Timestamp of the AIS record
IMO	International Maritime Organization number
MMSI	Maritime Mobile Service Identity
speed	Vessel sailing speed (knots)
latitude	Latitude of the vessel's position
longitude	Longitude of the vessel's position
head	Vessel heading direction
draught	Vessel draught depth
destination	Destination port name
ETA	Estimated Time of Arrival reported by captain

position, speed, course, and destination port, while simultaneously receiving similar information from surrounding vessels. AIS data records the real-time position of vessels, used for vessel tracking. Typical AIS data fields and their meanings are shown in Table 12.

Port geofence data records important spatial attributes of ports, including port locations, terminals, anchorage zones, pilot zones and berth boundaries. The data fields are summarized in Table 13. The anchorage, pilot and berth boundaries can be combined with vessel position from raw AIS data to determine the vessel's current behavior and operational status.

Table 13 Port geofence data fields and descriptions

Column name	Description
portName	Port name
portId	Unique port identifier
tnmList	List of terminal identifiers
prkList	List of berth identifiers
waitingArea	Anchorage area boundary
pilotArea	Pilotage area boundary
parkingArea	Berth area boundary

Static vessel information consists of the physical and operational characteristics of containers, such as vessel length, width, carrier, and maximum capacity. The main fields are summarized in Table 14. By combining static vessel information with raw AIS data, it becomes possible to analyze the navigation behavior and preferences of different types of vessels.

B. Baseline Model Hyperparameter Settings

This appendix summarizes the key hyperparameters used for all baseline models evaluated in this study. The configurations are reported to ensure reproducibility and to provide transparency regarding model capacity and regularization choices. All hyperparameters were fixed across experiments unless otherwise stated. The details are shown in Tables 15–20.

Table 14 Vessel static feature data fields and their descriptions

Column name	Description
IMO	International Maritime Organization number
MMSI	Maritime Mobile Service Identity
crrName	Vessel carrier company
TEU	Maximum container capacity
width	Vessel width
length	Vessel length

Table 15 Hyperparameter configuration of the LightGBM baseline.

Hyperparameter	Value
Objective function	MAE
Evaluation metric	MAE
Number of boosting rounds	1581
Learning rate	0.0133
Maximum tree depth	15
Number of leaves	16140
L1 regularization (λ_1)	0.0190
L2 regularization (λ_2)	0.0183

Table 16 Hyperparameter configuration of the XGBoost baseline.

Hyperparameter	Value
Objective function	Squared error regression
Number of estimators	1581
Learning rate	0.0133
Maximum tree depth	15
L1 regularization (α)	0.0190
L2 regularization (λ)	0.0183
Tree construction method	Histogram-based

Table 17 Hyperparameter configuration of the CatBoost baseline.

Hyperparameter	Value
Loss function	MAE
Number of trees	1000
Tree depth	15
Learning rate	0.1

Table 18 Configuration of the stacking ensemble baseline.

Component	Description
Base learners	LightGBM, XGBoost, CatBoost
Base learner hyperparameters	Identical to Tables 15–17
Meta-learner	Linear regression
Training strategy	Out-of-fold prediction on training set

Table 19 Hyperparameter configuration of the LSTM baseline.

Hyperparameter	Value
Hidden dimension	64
Number of LSTM layers	2
Embedding dimension	16
Dropout rate	0.1

Table 20 Hyperparameter configuration of the iTransformer baseline.

Hyperparameter	Value
Model dimension	64
Embedding dimension	8
Number of transformer layers	1
Number of attention heads	8
Feedforward dropout	0.1
Attention dropout	0.1

References

Abdi, A., Amrit, C., 2024. Enhancing vessel arrival time prediction: A fusion-based deep learning approach. *Expert Systems with Applications* 252, 123988.

Alessandrini, A., Mazzarella, F., Vespe, M., 2019. Estimated time of arrival using historical vessel tracking data. *IEEE Transactions on Intelligent Transportation Systems* 20, 7–15.

Chu, Z., Yan, R., Wang, S., 2024a. Are vessel arrival and port operations affected by covid-19? evidence from the hong kong port. *Transport Policy* 154, 157–181.

Chu, Z., Yan, R., Wang, S., 2024b. Evaluation and prediction of punctuality of vessel arrival at port: a case study of hong kong. *Maritime Policy & Management* 51, 1096–1124.

Chu, Z., Yan, R., Wang, S., 2025. Vessel arrival time to port prediction via a stacked ensemble approach: Fusing port call records and ais data. *Transportation Research Part C: Emerging Technologies* 176, 105128.

Derrow-Pinion, A., She, J., Wong, D., Lange, O., Hester, T., Perez, L., Nunkesser, M., Lee, S., Guo, X., Wiltshire, B., Battaglia, P.W., Gupta, V., Li, A., Xu, Z., Sanchez-Gonzalez, A., Li, Y., Velickovic, P., 2021. Eta prediction with graph neural networks in google maps, in: *Proceedings of the 30th ACM International Conference on Information and Knowledge Management*, ACM. p. 3767–3776.

El Mekkaoui, S., Benabbou, L., Berrado, A., 2022a. Deep learning models for vessel's eta prediction: bulk ports perspective. *Flexible Services and Manufacturing Journal* 35.

El Mekkaoui, S., Benabbou, L., Berrado, A., 2022b. Machine learning models for efficient port terminal operations: Case of vessels' arrival times prediction. *IFAC-PapersOnLine* 55, 3172–3177.

Jiang, S., Liu, L., Peng, P., Xu, M., Yan, R., 2025. Prediction of vessel arrival time to port: a review of current studies. *Maritime Policy & Management* 0, 1–26.

Kolley, L., Rückert, N., Kastner, M., Jahn, C., Fischer, K., 2023. Robust berth scheduling using machine learning for vessel arrival time prediction. *Flexible services and manufacturing journal* 35, 29–69.

Kwun, H., Bae, H., 2021. Prediction of vessel arrival time using auto identification system data. *Int J Innov Comput Inf Control* 17, 725–734.

Lee, H.T., Yang, H., Cho, I.S., 2021. Data-driven analysis for safe ship operation in ports using quantile regression based on generalized additive models and deep neural network. *Sensors (Basel, Switzerland)* 21.

Lei, J., Chu, Z., Wu, Y., Liu, X., Luo, M., He, W., Liu, C., 2024. Predicting vessel arrival times on inland waterways: A tree-based stacking approach. *Ocean Engineering* 294, 116838.

Liu, H., Jiang, W., Liu, S., Chen, X., 2023. Uncertainty-aware probabilistic travel time prediction for on-demand ride-hailing at didi, in: *Proceedings of the 29th ACM SIGKDD Conference on Knowledge Discovery and Data Mining*, pp. 4516–4526.

Liu, Y., Hu, T., Zhang, H., Wu, H., Wang, S., Ma, L., Long, M., 2024. itransformer: Inverted transformers are effective for time series forecasting. [arXiv:2310.06625](https://arxiv.org/abs/2310.06625).

Miao, H., Zhao, Y., Guo, C., Yang, B., Zheng, K., Huang, F., Xie, J., Jensen, C.S., 2024. A unified replay-based continuous learning framework for spatio-temporal prediction on streaming data. [arXiv:2404.14999](https://arxiv.org/abs/2404.14999).

Noman, A.A., Heuermann, A., Wiesner, S., Thoben, K.D., 2025. A review of vessel time of arrival prediction on waterway networks: Current trends, open issues, and future directions. *Computers* 14, 41.

Noman, A.A., Heuermann, A., Wiesner, S.A., Thoben, K.D., 2021. Towards data-driven gru based eta prediction approach for vessels on both inland natural and artificial waterways, in: *2021 IEEE International Intelligent Transportation Systems Conference (ITSC)*, IEEE Press. p. 2286–2291.

Ogura, T., Inoue, T., Uchihira, N., 2021. Prediction of arrival time of vessels considering future weather conditions. *Applied Sciences* 11.

Park, K., Sim, S., Bae, H., 2021. Vessel estimated time of arrival prediction system based on a path-finding algorithm. *Maritime Transport Research* 2, 100012.

Servos, N., Liu, X., Teucke, M., Freitag, M., 2019. Travel time prediction in a multimodal freight transport relation using machine learning algorithms. *Logistics* 4, 1.

UNCTAD, 2024. Review of maritime transport 2024. https://unctad.org/system/files/official-document/rmt2024_en.pdf. (Accessed 25 May 2025).

Vaswani, A., Shazeer, N., Parmar, N., Uszkoreit, J., Jones, L., Gomez, A.N., Kaiser, L., Polosukhin, I., 2023. Attention is all you need. [arXiv:1706.03762](https://arxiv.org/abs/1706.03762).

Wang, H., Yan, R., Wang, S., Zhen, L., 2023. Innovative approaches to addressing the tradeoff between interpretability and accuracy in ship fuel consumption prediction. *Transportation Research Part C: Emerging Technologies* 157, 104361.

Wenzel, P., Jovanovic, R., Schulte, F., 2023. A neural network approach for eta prediction in inland waterway transport, in: *Computational Logistics*, Springer Nature Switzerland, Cham. pp. 219–232.

Wenzhe, J., Haina, T., Xudong, Z., 2025. Stgdpm:vessel trajectory prediction with spatio-temporal graph diffusion probabilistic model. [arXiv:2503.08065](https://arxiv.org/abs/2503.08065).

Yan, R., Wang, S., Zhen, L., Laporte, G., 2021. Emerging approaches applied to maritime transport research: Past and future. *Communications in Transportation Research* 1, 100011.

Yang, Y., Yan, R., Wang, S., 2024. An efficient ranking-based data-driven model for ship inspection optimization. *Transportation Research Part C: Emerging Technologies* 165, 104731.

Yuan, Y., Shao, C., Ding, J., Jin, D., Li, Y., 2024. Spatio-temporal few-shot learning via diffusive neural network generation, in: *The Twelfth International Conference on Learning Representations*.

Zhang, X., Fu, X., Xiao, Z., Xu, H., Wei, X., Koh, J., Ogawa, D., Qin, Z., 2023. Prediction of vessel arrival time to pilotage area using multi-data fusion and deep learning, in: *2023 IEEE 26th International Conference on Intelligent Transportation Systems (ITSC)*, pp. 2268–2268.